



HAL
open science

Plasma properties conditioned by the magnetic throat location in a helicon plasma device

Alfio E Vinci, Stéphane Mazouffre

► **To cite this version:**

Alfio E Vinci, Stéphane Mazouffre. Plasma properties conditioned by the magnetic throat location in a helicon plasma device. *Journal of Applied Physics*, 2021, 130 (18), pp.183301. 10.1063/5.0069983 . hal-03474101

HAL Id: hal-03474101

<https://hal.science/hal-03474101v1>

Submitted on 10 Dec 2021

HAL is a multi-disciplinary open access archive for the deposit and dissemination of scientific research documents, whether they are published or not. The documents may come from teaching and research institutions in France or abroad, or from public or private research centers.

L'archive ouverte pluridisciplinaire **HAL**, est destinée au dépôt et à la diffusion de documents scientifiques de niveau recherche, publiés ou non, émanant des établissements d'enseignement et de recherche français ou étrangers, des laboratoires publics ou privés.

1 Plasma properties conditioned by the magnetic throat location 2 in a Helicon plasma device

3 Alfio E Vinci^{a)} and Stéphane Mazouffre^{b)}

4 *Institut de Combustion, Aérodynamique, Réactivité et Environnement (ICARE), Centre National de la Recherche Scientifique,*
5 *1C Avenue de la Recherche Scientifique, 45071 Orléans, France*

6 (Dated: 21 September 2021)

Measurements are conducted in a Helicon plasma device to analyze the spatial distribution of plasma properties as the throat of the magnetic nozzle is axially shifted with respect to the antenna center. Krypton plasma is generated in the sub-kilowatt range and probed using a suite of diagnostics including a rf-compensated Langmuir probe, a planar probe and laser-induced fluorescence. It is found that larger ion currents and increased plasma confinement are achieved when the throat of the magnetic nozzle is located downstream the antenna center, at a distance that equals or exceeds two times the antenna length. The ions, although being accelerated, retain subsonic velocities even beyond the magnetic throat.

7 I. INTRODUCTION

8 A recent keen interest in electric space propulsion stems
9 from an increasing number of small satellites being deployed
10 for plural applications^{1–6}. Simple and compact thrusters can
11 allow for in-space maneuvering of such small spacecrafts⁷
12 which usually do not boast large volume capacity to meet the
13 needs of consolidated technologies, e.g. Gridded Ion thrusters
14 and Hall thrusters. As a result, a portion of research and devel-
15 opment efforts are being focused on electrodeless devices and
16 magnetic nozzle (MN) acceleration^{8–13}. This kind of technol-
17 ogy can indeed offer a number of advantages compared to the
18 aforementioned state-of-the-art devices. Issues linked to ero-
19 sion of components are expected to be of little consequence
20 due to the absence of direct interaction between plasma dis-
21 charge and electrodes, resulting in a long lifetime. The plasma
22 beam leaving the discharge chamber is quasineutral, thus no
23 neutralizer is required. Furthermore, these plasma sources
24 can more easily operate using condensable propellants with
25 respect to those system that require a dedicated neutralizer,
26 whose lifetime and reliable functioning can be considerably
27 affected¹⁴.

28 The Helicon plasma (HP) thruster is one such a device. It
29 mainly comprises three components: *i*) a dielectric tube as
30 plasma discharge region, *ii*) a radiofrequency (rf) antenna for
31 gas ionization and *iii*) an axially directed steady magnetic field
32 for plasma confinement and expansion throughout its diverg-
33 ing region, i.e. the magnetic nozzle. Power radiated by the an-
34 tenna is deposited in the electron population as thermal energy
35 by means of helicon wave modes¹⁵ and Trivelpiece–Gould
36 wave modes¹⁶. The energy is used for plasma production and
37 transport phenomena, such as ambipolar electric field, result-
38 ing in axial acceleration of the ions in the MN by conversion
39 of the electron thermal energy.

40 The maturity of this technology is still relatively low⁵,
41 whereby several undesired aspects come along with the con-
42 sidered advantages. The most critical one perhaps regards the

43 thrust efficiency. Thus far, direct thrust measurements have
44 revealed efficiencies typically below 10% in many different
45 devices^{13,17–24}, with the only recent exception of nearly 20%
46 at several kW of input power¹². In this scenario, improv-
47 ing the attained performance is required in order to turn HP
48 thrusters into a competitive technology in the near future. The
49 better understanding of the physics governing such rf plasma
50 sources by exploring the different working parameters is cur-
51 rently the preferred approach to provide an exhaustive opti-
52 mization pathway.

53 In an effort to model HP discharges, previous analy-
54 ses have considered different magnetic topologies inside
55 the source tube, e.g. uniform^{25,26}, Helmholtz and Maxwell
56 configurations²⁷. The magnetic field inside the source is then
57 matched with a divergent geometry through a magnetic throat
58 localized in the proximity of the tube exit. This firm condi-
59 tion is not necessarily the most convenient solution, as demon-
60 strated in Ref. 28 where a stepped-diameter tube is employed
61 and the magnetic throat is placed downstream the exit cross
62 section of the small main tube. Besides, virtually every nu-
63 merical and experimental work studying the influence of mag-
64 netic nozzle on the plasma properties, limited the analysis to
65 the exploitation of different magnitudes at the throat. A fruit-
66 ful investigation is reported in Ref. 29, where the location of
67 the magnetic throat is indirectly shifted with respect to the an-
68 tenna – which is constantly located at the back plate – by
69 changing the discharge tube length. Another relevant analy-
70 sis is reported in Ref. 30, where the authors characterized the
71 plasma and the rf power circuit when the magnetic throat lo-
72 calized either within the source or at the exhaust. Bennet *et*
73 *al.*³¹ studied the generation of plasma as a function of the MN
74 throat location. Yet, their setup did not include plasma expan-
75 sion outside the discharge tube and many operating conditions
76 relied on magnetized ions, which is not a typical scenario in
77 propulsion. The shape of the magnetic nozzle and the location
78 of the throat are presumably strongly linked to the amount
79 of the input energy that can be usefully converted into axial
80 thrust. Energetic electrons are mainly produced close to the
81 region occupied by the antenna. Several phenomena occur
82 in the nozzle, such as transport due to pressure gradient and
83 electron cooling via convection and/or conduction, which de-
84 termine the conversion efficiency of inlet thermal energy into

^{a)}alfio.vinci@cns-orleans.fr

^{b)}stephane.mazouffre@cns-orleans.fr

This is the author's peer reviewed, accepted manuscript. However, the online version of record will be different from this version once it has been copyedited and typeset.
PLEASE CITE THIS ARTICLE AS DOI: 10.1063/5.0069983

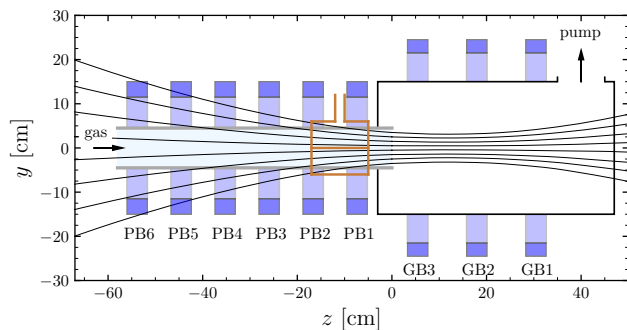


FIG. 1. Helicon source schematics. The $z = 0$ position refers to the discharge tube outlet, $y = 0$ refers to the reactor axis.

ion acceleration. Furthermore, as the throat is shifted along the thruster axis with respect to the antenna location, the expansion ratio of the plasma beam changes, thus resulting in possibly different thrust levels.

This paper reports on experimental results obtained in a HP source operating with krypton under several configurations of the external magnetic field. Numerous plasma properties are spatially resolved as the throat of the magnetic field is moved with respect to the antenna axial position. A detailed description of the experimental setup is provided in Section II, including the HP source and the magnetic configurations. In Section III, the diagnostics are extensively described. They include: a rf-compensated Langmuir probe to spatially characterize plasma density, electron temperature, and plasma potential; a planar probe to measure the ion current density; laser-induced fluorescence to explore the axial ions and atoms velocity distribution function. Measurements are presented and discussed in Section IV. Eventually, conclusions are drawn in Section V.

II. EXPERIMENTAL SETUP

A schematics of the HP source employed in this study is shown in Figure 1 along with an example of computed magnetic field lines. The entire experimental setup is oriented in a vertical position.

The discharge chamber consists in a borosilicate glass tube with $\phi = 9$ cm inner diameter and $L = 58$ cm length, whose open exit arbitrarily identifies the origin of the axial coordinate z . Krypton gas is introduced off-axis in the tube through its top aperture at a nominal flow rate of 1 ± 0.004 mg s⁻¹. The bottom part is connected to a 30 cm in inner diameter and 50 cm in length expansion chamber made in aluminum which is equipped with a turbomolecular/primary pumping system. The ultimate base pressure is in the order of 10^{-5} mbar, whereas the typical pressure during operation reads $\sim 5 \times 10^{-3}$ mbar.

The rf antenna in use is a double-saddle type with $d_A = 12$ cm length centered at $z \cong -11$ cm. It is made of pure copper and features two feeding arms which are long enough to be directly connected to the matching network so

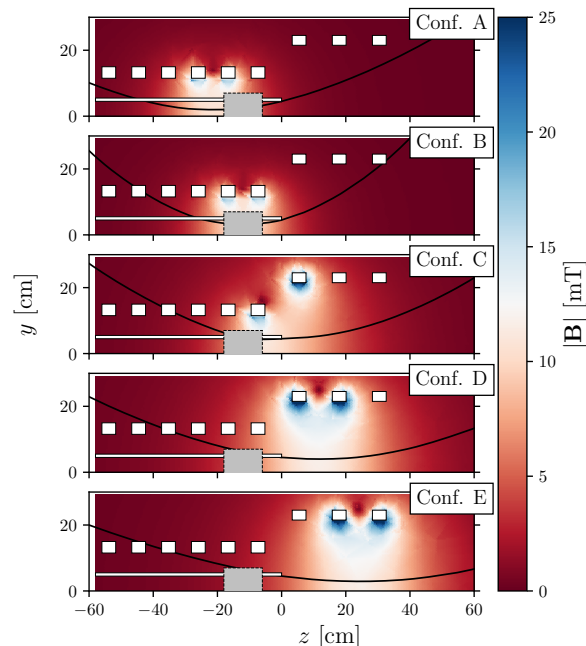


FIG. 2. 2D profiles of the externally applied magnetic fields. White line indicates the discharge tube walls, white rectangles represent the magnetic coils, the gray rectangle indicates the antenna region and the black solid line exemplifies the magnetic streamline crossing the tube edge at $z = 0$.

that power losses due to intermediate links are prevented. Input rf power is generated by a 1 kW-class power supply at 13.56 MHz and kept constant to 750 W throughout the reported measurements. The power carried by higher order harmonics is certified to be lower than -40 dBc. Matching of the rf power is attained via a custom π -type network. During operation, values of the reflected power are below ~ 2 %.

A set of nine electromagnets surrounds both the discharge tube and the expansion chamber. Their denomination is reported in Figure 1. Each electromagnet is made up of a 2 mm diameter copper wire, constituting 510 loops for PB1-6 and 430 loops for GB1-3. The presence of multiple electromagnets enables the investigation of profoundly different magnetic field topologies. For the purpose of this study, five magnetic configurations are examined by powering two electromagnets at once. In doing so, the location of the magnetic throat is intentionally relocated along the z axis. The tested magnetic configurations are progressively labeled as Conf. A to Conf. E. When involved, PB coils are powered with 3 A and GB coils with 6 A of direct current. Figure 2 shows the computed 2D magnetic field maps, highlighting the streamline that crosses the discharge tube edge at $z = 0$, thus defining the ideal shape of the plasma plume (whether it is assumed fully magnetized). With reference to Figure 2, it is noteworthy to emphasize on the magnetic throat location. It moves from upstream the antenna in Conf. A to far downstream the an-

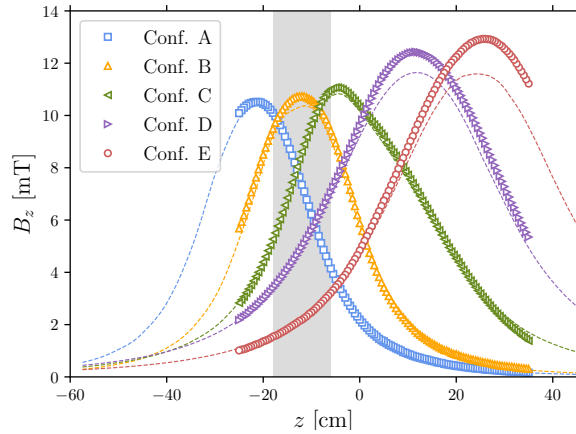


FIG. 3. Externally applied magnetic field on-axis profiles. Shaded area indicates the antenna location. Dashed lines represent simulation profiles, scatter points indicate probe measurements.

150 tenna in Conf. E. The first axial mode the antenna can generate
 151 translates in an axial wavelength as $\lambda_z = 24$ cm, see Section
 152 IV C. Notice that the magnetic throat in Conf. D is approxi-
 153 mately one wavelength downstream of the antenna center. The
 154 magnitude of the on-axis magnetic field is reported in Figure
 155 3 by comparing computed values and measured values. All
 156 magnetic configurations feature a peak value of $10 \div 13$ mT
 157 with a similar qualitative profile but shifted along z .

158 III. DIAGNOSTICS

159 A. RF-compensated Langmuir probe

160 Plasma density n_p , electron temperature T_e and plasma po-
 161 tential V_p are measured using a rf-compensated Langmuir
 162 probe (LP), see Figure 4. A detailed description of the probe
 163 has been previously reported in¹¹. It is designed in accord-
 164 ance with the results reported in³²⁻³⁴. A tungsten wire of
 165 0.38 mm in diameter and 5 mm in length constitutes the probe
 166 tip. An additional electrode made of stainless steel contributes
 167 to rf compensation and provides mechanical support to the as-
 168 sembly. The electrode is electrically insulated from the probe
 169 tip using a 1 mm in outer diameter alumina tube. A 1 nF axi-
 170 al capacitor is soldered to the compensation electrode and
 171 connected in parallel with the probe tip and a series of three
 172 axial chokes, each of which self-resonates at one of the first
 173 three harmonics. The whole assembly is encapsulated inside
 174 a borosilicate glass tube of 6 mm outer diameter, which also
 175 accommodates the coaxial cable for probe biasing and current



FIG. 4. RF-compensated Langmuir probe.

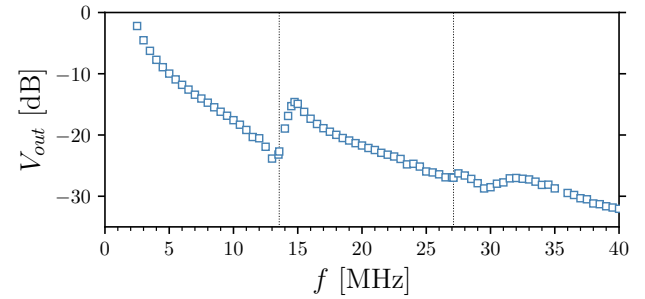


FIG. 5. RF-compensated LP frequency spectrum ($V_{ref} = 10$ V). Vertical dotted lines indicate 13.56 MHz and 27.12 MHz.

176 measuring.

177 Chokes selection is attained by characterization of their
 178 impedance frequency spectrum. A $20 V_{pp}$ sinewave is gener-
 179 ated by a function generator and fed to one lead of the testing
 180 choke. The other lead is connected to a 46.52 k Ω resistor and
 181 the series circuit closes to the ground. The frequency of the
 182 input sinewave is swept while the voltage drop across the re-
 183 sistor is monitored and used to calculate the current flowing
 184 in the circuit. The frequency at which the current is minimum
 185 is the choke self-resonating frequency. Functional check of
 186 the whole probe assembly is performed by applying a $20 V_{pp}$
 187 sinewave to the tungsten tip at different frequencies. The
 188 probe output is recorded by a digital oscilloscope and shown
 189 in Figure 5 as a function of the input frequency. Local minima
 190 are evident in correspondence of the harmonic frequencies, as
 191 desired.

192 The probe is manually displaced within the plasma using
 193 a single-axis translation stage with a resolution of 10 μ m and
 194 a stroke of 150 mm. Probe alignment is ensured by the use
 195 of a cross-line laser pendulum. I-V curves are recorded us-
 196 ing a ALP control unit by Impedans Ltd. Thereafter, data is
 197 post-processed relying on OML theory^{34,35}. Assuming local
 198 quasineutrality, plasma density n_p is inferred from the linear
 199 fit of the ion current squared versus the probe potential. The
 200 ion current fit is then subtracted from the total current to ob-
 201 tain a better estimation of the electron current. Assuming the
 202 electrons are described by a Maxwell-Boltzmann distribution
 203 function, the logarithmic profile of the electron current is lin-
 204 early fitted, enabling the estimation of the electron tempera-
 205 ture T_e . The plasma potential V_p is computed as the probe bias
 206 voltage where the first derivative of the I-V curve features its
 207 peak value.

208 Uncertainty associated with the probe measurements is es-
 209 timated through a statistical approach. The detailed procedure
 210 has been previously reported in¹¹. The outline of the analysis
 211 shows that all plasma parameters are measured with a statisti-
 212 cal deviation as high as ~ 2 %.

213 B. Planar probe with guard ring

214 The ion current density j_i is measured using a planar probe
 215 with a guard ring (PPGR). It mainly comprises a disk-shaped

This is the author's peer reviewed, accepted manuscript. However, the online version of record will be different from this version once it has been copyedited and typeset.
PLEASE CITE THIS ARTICLE AS DOI: 10.1063/1.50069983

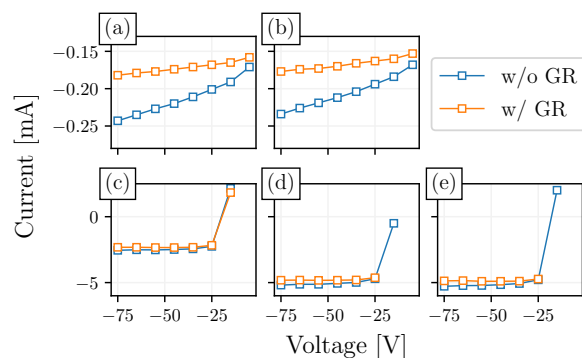


FIG. 6. Ion current profiles at $(x, y = 0; z = 15 \text{ cm})$. Subplots denomination is linked to magnetic configurations Conf.s A-E.

216 collector and an outer ring, both made in stainless steel. The
217 role of the guard ring is to concentrate sheath edge effects far
218 from the collector, thus ensuring that the ion collection area
219 exactly corresponds to the collector geometrical area³⁶. For
220 correct functioning of the probe, it is required that *i*) the width
221 of the guard ring is much larger than the local plasma sheath
222 thickness and *ii*) the gap between the two electrodes is smaller
223 than the local sheath thickness to introduce negligible poten-
224 tial irregularities. The collector is 5.6 mm in diameter and
225 1 mm in thickness, whereas the ring width is 1 mm. A gap
226 of 100 μm is maintained between the two electrodes to ensure
227 electrical insulation. Each electrode features a separated elec-
228 trical connection for polarization and current measurement.
229 Voltage is applied to the collector by way of a Keithley 2410
230 SourceMeter, which is also used to measure the flowing cur-
231 rent. The guard ring is biased using a TTIEX752M power
232 supply.

233 Functional check of the probe is carried out by recording
234 the I-V curves at $(x, y = 0; z = 15 \text{ cm})$ for the five magne-
235 tic configurations denominated Conf.s A-E. The curves obtained
236 with a biased and floating guard ring are compared in Figure
237 6. Saturation of the ion current is achieved for Conf.s C-D-E
238 at voltages lower than about -40 V , while no complete satu-
239 ration is recorded for Conf.s A and B due to the fact that the
240 guard ring width is not compatible with the local values of
241 the sheath thickness. This can be confirmed by computing the
242 local values of the characteristic lengths over the radial coor-
243 dinate using the values of n_p and T_e later discussed in Section
244 IV. Floating and high voltage sheath thickness, s_f and s_{hv} re-
245 spectively, are computed in accordance with³⁷, using -75 V
246 for Conf.s A-B and -50 V for Conf.s C-D-E. Outcomes are
247 plotted in Figure 7. It results evident that values of s_{hv} for
248 Conf.s C-D-E are much smaller than the guard ring width,
249 whereas those for Conf.s A and B approach its size. It shall
250 be noted that the attainment of a perfectly flat profile of the
251 ion saturation current would require a guard ring width $5 \div 10$
252 times larger than the actual one. Thus, the overall probe size
253 would probably lead to serious plasma perturbations. Further-
254 more, the scope of the presented measurements is not to, e.g.,
255 focus on indirect propulsive performance estimation but rather

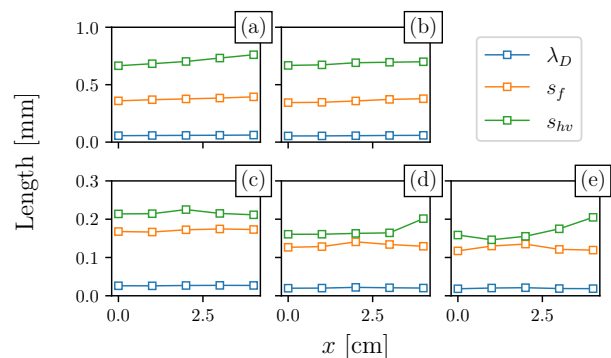


FIG. 7. Debye length, floating and high-voltage sheath thickness at $z = 15 \text{ cm}$. Subplots denomination is linked to magnetic configurations Conf.s A-E.

256 to perform a more qualitative-like comparison of the five mag-
257 netic configurations.

258 Given the high level of reproducibility recorded during pre-
259 liminary measurements, the uncertainty in j_i is mainly given
260 by the uncertainty in the measured current and the probe col-
261 lecting area. This consideration leads to a value of $< 8 \%$.

262 The planar probe is manually actuated from outside the
263 chamber using the single-axis translation stage described in
264 Section III A.

265 C. Laser-induced fluorescence setup

266 Ions and atoms velocity distribution functions (VDFs) are
267 measured by means of laser-induced fluorescence (LIF) spec-
268 troscopy. The technique and the optical bench in use have
269 been extensively described in previous works^{38,39}. Excita-
270 tion of metastable levels is achieved via an amplified tunable
271 single-mode laser diode in the 810 – 840 nm spectral range.
272 The primary laser beam is split in multiple beams with the
273 purpose of *i*) instantaneous monitoring of the laser mode and
274 detection of any mode hop by means of a Fabry-Pérot inter-
275 ferometer, *ii*) laser power check using a photodiode and *iii*) ac-
276 curate wavelength measurement by way of a calibrated waveme-
277 ter whose absolute uncertainty is $\sim 60 \text{ m s}^{-1}$ (80 MHz). Mod-
278 ulation of the laser beam is achieved using a mechanical chop-
279 per at $\sim 1.9 \text{ kHz}$. The laser is coupled to a 50 μm optical
280 fiber which allows transporting the laser beam from the optical
281 bench to the Helicon source setup. Laser is injected inside the
282 vacuum chamber through a borosilicate glass window located

TABLE I. Kr I and Kr II probed optical transitions.

	Transition	λ_{exc} [nm] (vacuum)	λ_{fluo} [nm] (air)
Kr I	$5s^2[3/2]_1^o \rightarrow 5p^2[3/2]_2$	819.23095	760.15457
Kr II	$5p^2D_{5/2}^o \rightarrow 5s^2P_{3/2}$	820.4959	461.91658

This is the author's peer reviewed, accepted manuscript. However, the online version of record will be different from this version once it has been copyedited and typeset.
PLEASE CITE THIS ARTICLE AS DOI: 10.1063/5.0069983

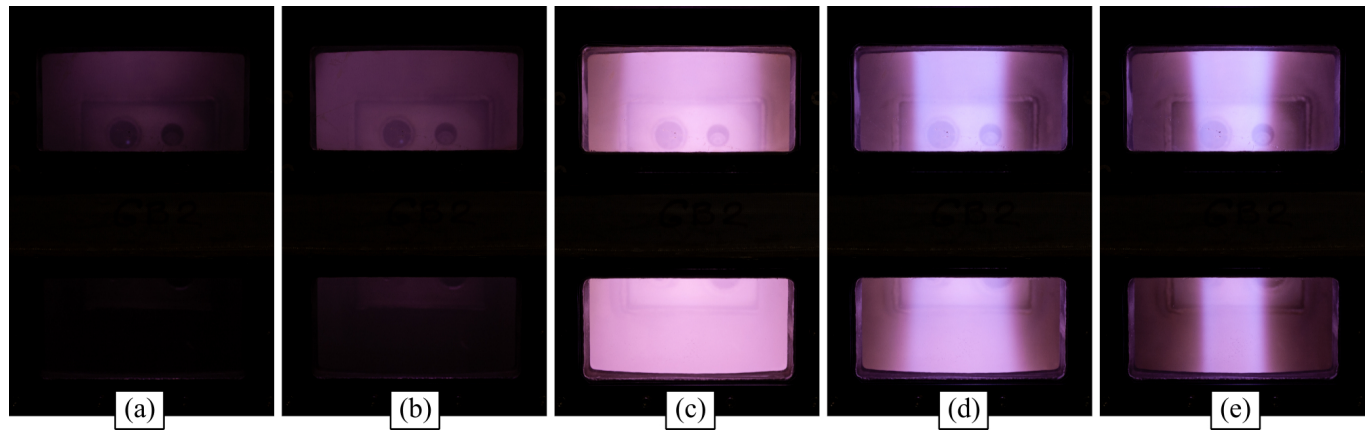


FIG. 8. Photographs of the plasma plume in (a) Conf. A, (b) Conf. B, (c) Conf. C, (d) Conf. D and (e) Conf. E. Windows are centered at $z = 12$ and $z = 24$ cm.

at the bottom of the reactor. Note that $\mathbf{k} \cdot \mathbf{v} < 0$ here, where \mathbf{k} is the laser wavenumber and \mathbf{v} the particle velocity. The laser beam is collimated using a combination of a 150 mm and a 1000 mm focal length plano-convex lenses. Uncertainty on the alignment with respect to the HP source axis is estimated to be $\lesssim 1.6$ deg. In order to ensure a linear regime of the studied optical transitions, the laser power density delivered to the plasma is kept below 1.2 W mm^{-2} , a threshold value that has been determined during preliminary measurements. A detection branch is placed perpendicularly to the excitation beam featuring a pair of plano-convex lenses (250 mm and 100 mm focal lengths) focusing on a $200 \mu\text{m}$ core diameter optical fiber. Both the excitation and detection branches are mounted on a dedicated computer-controlled high precision linear translation stage to enable spatially resolved measurements along the y axis. The detection optical train can be additionally displaced along the z axis within a few centimeters using a manual stage. The $200 \mu\text{m}$ optical fiber transports the fluorescence light to a monochromator which isolates the desired line from the whole spectrum. Afterwards, a photomultiplier tube is used to convert the light signal into voltage, which is fed into a lock-in amplifier operating at the laser modulation frequency to distinguish the signal from the natural plasma emission. The VDFs are inferred by scanning over the laser wavelength λ and computing the particles axial velocity v_z as $v_z = c(\lambda - \lambda_0)/\lambda_0$, where λ_0 is the unshifted transition wavelength and c is the speed of light. The measured LIF profiles result from the Doppler broaden line. The presence of Kr isotopes leads to broadening due to isotopic shift and hyperfine structure³⁸. Moreover, due to the presence of a steady magnetic field, the Zeeman effect splits the spectral lines into sub-levels³⁸. Nevertheless, since the spectrum is dominated by the ^{84}Kr isotope and the magnetic field is relatively weak, it is herein assumed that the observed fluorescence line profile images the local VDF.

The probed optical transitions are reported in Table I. The zero-velocity wavelength for Kr I is estimated from preliminary measurements in the HP source shining the laser along the x axis. The other listed wavelengths are given in the literature^{38–42}.

IV. EXPERIMENTAL RESULTS AND DISCUSSION

A. Visual inspection

The very first piece of information regarding the way the plasma responds to the applied magnetic field topology is provided by visual inspection. The photographs of the plasma plume reported in Figure 8 are taken using a common DSLR camera framing the region $8 < z < 28$ cm and set at $f/8$ and $1/40$ s exposure time. It results evident how significant differences characterize the extracted plasma plume when employing the different magnetic topologies. A faint plume is visible when the reactor operates in Conf. A and Conf. B. Instead, a well defined plasma beam is noticed when Conf.s C, D and E are chosen. In the latter cases, the plasma radius visibly delineates the local magnetic streamlines, cf. Figure 2 and Figure 8. It is interesting to notice that the local magnitude of the axial component B_z is nearly equal for Conf. C and Conf. E at $z = 12$ cm (see Figure 2), i.e. at the center of the top window in Figure 8. Yet, the two plasma beams show a very different structure. As a matter of fact, local values of the field radial component B_r and gradient $\partial B_z / \partial z$ significantly differ. This finding agrees with previous numerical models^{26,43} and intrinsically points out that both $|\mathbf{B}|$ and $\nabla \mathbf{B}$ have an impact on the plasma behavior.

B. LP measurements

Plasma properties are characterized using the diagnostics described in Section III. The region delimited by $0 < y < 4$ cm and $-4 < z < 21$ cm is probed by means of the rf-compensated LP. I-V characteristics are recorded with a spatial resolution of 5 mm. Data is post-processed as discussed in Section III A and eventually interpolated to enhance visualization. Figures 9, 10 and 11 illustrate normalized 2D maps of n_p , T_e and V_p , respectively, for the five magnetic topologies. Normalization values are: $6 \times 10^{17} \text{ m}^{-3}$ as regards to n_p , 6 eV for T_e and 25 V for V_p . The solid black lines

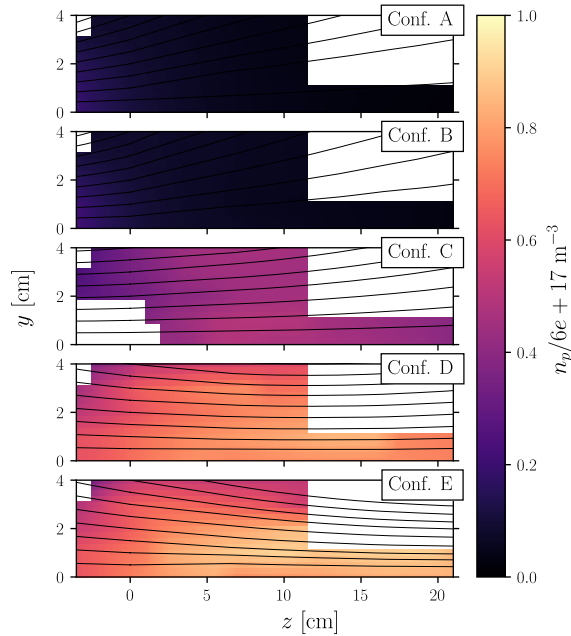


FIG. 9. Normalized plasma density for the five magnetic configurations. Normalization factor is $6 \times 10^{17} \text{ m}^{-3}$. Solid black lines represent magnetic streamlines.

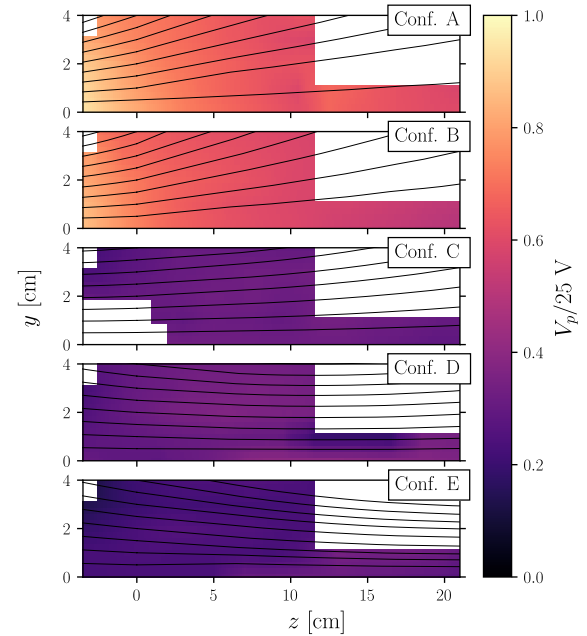


FIG. 11. Normalized plasma potential for the five magnetic configurations. Normalization factor is 25 V. Solid black lines represent magnetic streamlines.

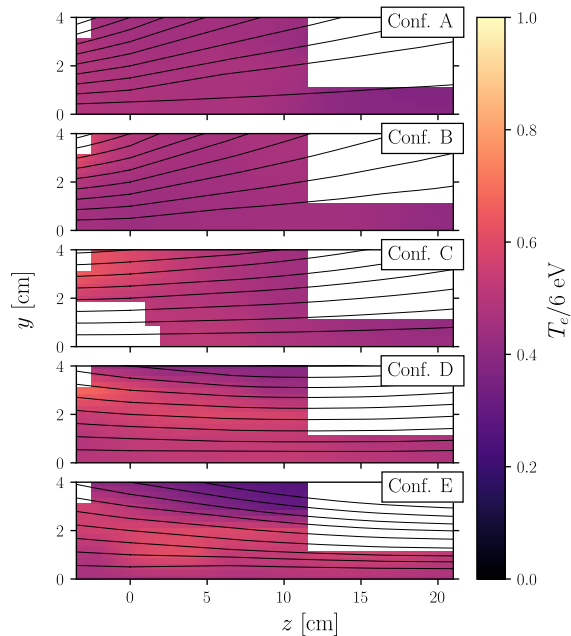


FIG. 10. Normalized electron temperature for the five magnetic configurations. Normalization factor is 6 eV. Solid black lines represent magnetic streamlines.

This is the author's peer reviewed, accepted manuscript. However, the online version of record will be different from this version once it has been copyedited and typeset.
PLEASE CITE THIS ARTICLE AS DOI: 10.1063/5.0069983

357 included in the figures represent the magnetic streamlines de-
358 limited by the discharge tube edge at $z = 0$. Furthermore, on-
359 axis profiles of n_p , T_e and V_p are shown in Figure 12. These
360 experimental measurements show that:

- 361 1. when the HP source operates in Conf. A, the extracted
362 plasma plume is characterized by a low monotonically
363 decreasing profile of n_p ranging between $\sim 1 \times 10^{17}$
364 and $\sim 9 \times 10^{15} \text{ m}^{-3}$ along the reactor axis. The pro-
365 file of T_e features a monotonic behavior as well, with
366 a peak value of $\sim 3 \text{ eV}$. In a similar fashion, V_p drops
367 from $\sim 24 \text{ V}$ to $\sim 15 \text{ V}$. All plasma properties peak on-
368 axis at $z < 0$. These quantitative observations agree with
369 the faint light emitted in the nozzle region, as stated be-
370 forehand. Visual check of the plasma also reveals that
371 light is instead concentrated within the discharge tube.
372 It suggests that the radial and back boundaries represent
373 a major loss term of plasma^{26,44}.
- 374 2. when the HP source operates in Conf. B, analogous ar-
375 guments can be put forward. The profile of n_p like-
376 wise peaks on-axis at $z < 0$ and decays monotonically
377 downstream. Altogether, slightly larger values of n_p are
378 measured with respect to Conf. A. In the bulk of the
379 plasma, T_e remains in the order of $\sim 3 \text{ eV}$ with lower
380 values downstream. However, a population of relatively
381 more energetic electrons ($T_e \sim 3.5 \text{ eV}$) appears off-axis,
382 in correspondence of the magnetic nozzle edge, visible
383 at $z < 0$ in Figure 10(b). Although qualitatively very

- 384 similar, the distribution of V_p for Conf. B presents lower
385 values with respect to Conf. A of a few volts.
- 386 3. when the HP source operates in Conf. C, results similar
387 to those previously reported in¹¹ using the same HP
388 source are obtained. As a matter of fact, in both the ex-
389 periments the magnetic throat is located at $z = 0$. In
390 contrast to what was discussed in points (i) and (ii),
391 all plasma properties peak off-axis. Data acquisition
392 in the region ($0 < r < 2, z < 0$) was not possible due
393 to discharge instability possibly induced by the probe
394 presence. The largest value of n_p is recorded at $z > 0$
395 and it reads $\sim 3 \times 10^{17} \text{ m}^{-3}$, whereas T_e reaches a peak
396 of 4 eV at $z < 0$. The distribution of V_p is relatively
397 isotropic, ranging in the $8 \pm 0.5 \text{ V}$ interval. The rea-
398 son why n_p and T_e present separated regions of the re-
399 spective maximum values has been explained in^{11,45} in
400 terms of pressure balance. When considering the z com-
401 ponent of the electron momentum conservation equa-
402 tion in the limit of negligible contribution due to mo-
403 mentum transfer collisions and due to the Lorenz force,
404 the potential gradient and the pressure gradient balance
405 each other. In the region where $B_r/B_z \ll 1$, i.e. where
406 the local magnetic field divergence angle is small, the
407 reduced cross field electron mobility yields a relatively
408 large axial conductivity, resulting in a nearly null poten-
409 tial gradient. Hence, for equilibrium reasons, the pres-
410 sure gradient is required to be small, which results in
411 a larger n_p where T_e is lower and vice versa. Similar
412 results are numerically found and discussed in⁴⁶.
- 413 4. when the HP source operates in Conf. D, light emis-
414 sion upstream the antenna is almost absent, hinting that
415 plasma losses at the back and lateral walls are mitigated
416 with respect to the previous cases. With reference to
417 Figure 9(d), it is evident that n_p follows the axial gra-
418 dient of B_z . The maximum value of $\sim 5 \times 10^{17} \text{ m}^{-3}$
419 is therefore located in correspondence of the magnetic
420 throat. In Figure 10(d), it is relevant to notice the dis-
421 tinct transport pattern of a relatively more energetic
422 electron population along the magnetic field lines at the
423 edge of the nozzle, which exhibits $T_e \approx 3.5 \div 4.2 \text{ eV}$. A
424 relatively small V_p is measured throughout the probed
425 region, with a peak value in the order of 10 V in the
426 area of maximum n_p .
- 427 5. when the HP source operates in Conf. E, similar ob-
428 servations to those stated in point (4) can be raised.
429 Profiles of n_p and T_e have a strong dependence on the
430 spatial distribution of B_r and B_z . The highest plasma
431 density value among all the studied magnetic configura-
432 tions is herein recorded to be $\sim 5.5 \times 10^{17} \text{ m}^{-3}$ nearby
433 the magnetic throat. As highlighted in point (4), also
434 in this case a more energetic population of electrons is
435 transported along the external surface of the magnetic
436 nozzle, cf. Figure 10(e). At $z \cong 10 \text{ cm}$, all the electrons
437 with $T_e \gtrsim 3 \text{ eV}$ are concentrated in a radius of about
438 3 cm, as visually confirmed by Figure 8(e).

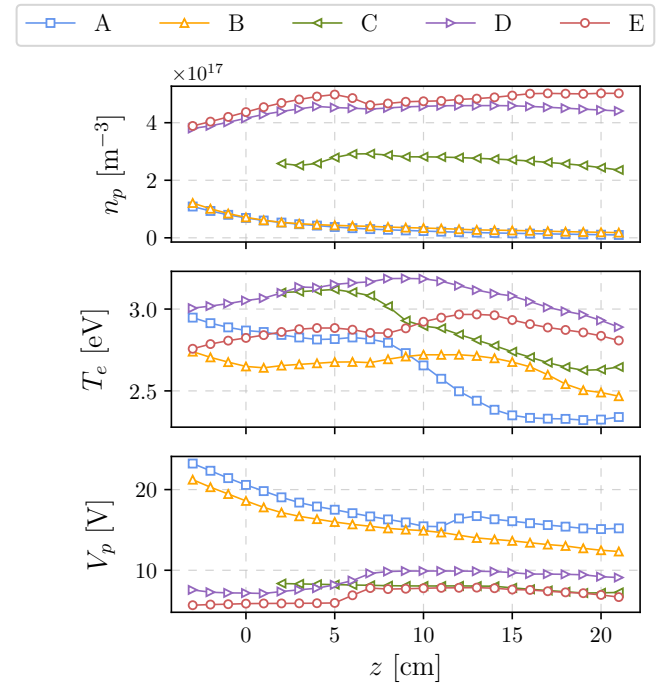


FIG. 12. On-axis profiles of (top) plasma density, (middle) electron temperature and (bottom) plasma potential. Data is extracted from Figures 9-11 and down-sampled to enhance visualization.

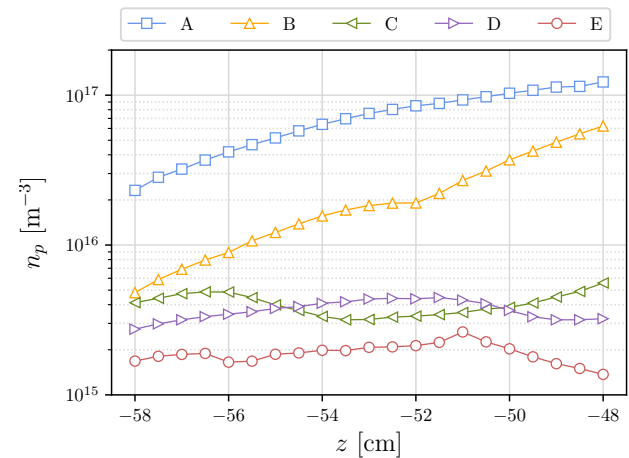


FIG. 13. Ion density profile in the proximity of the back-plate for the five magnetic configurations.

439 Eventually, it is worth observing that the different config-
440 urations of B possibly influence the power deposition map.
441 This, in turn, very likely relates to the different spatial distri-
442 butions of n_p and T_e as discussed in points (1)-(5).

443 In addition to the measurements performed using the rf-
444 compensated LP, a simple uncompensated LP is inserted on-
445 axis at the back/injection plate of the HP source to measure
446 n_p as an indicator of the plasma flux lost in this region. The
447 probe is biased to scan over the ion saturation branch only.

448 No significant distortions due to rf oscillations are expected in
449 this part of the I-V curve³³. For obtaining this particular set
450 of data, the reactor injection plate has been modified in order
451 to accommodate the probe and its related wiring. The pro-
452 pellant is still injected off-axis but it goes through a plenum
453 first and eventually reaches the discharge tube via a multi-
454 perforated surface, resulting in a axial gas flow. An uncom-
455 pensated probe is chosen due to limitations on the available
456 room. The measured profiles of n_p are shown in Figure 13
457 for Conf. A to E. Since the magnetic throat in Conf. A is lo-
458 cated upstream the antenna, the ions are mostly transported
459 towards the back plate by following the convergent-divergent
460 shape of the magnetic field. As the magnetic throat moves far-
461 ther downstream from the antenna center, lower densities are
462 measured in the proximity of the injection plate, as expected.

463 C. Plasma density profile model

464 Using a simplified description of the plasma, the measured
465 axial profiles of n_p can be compared with theoretical profiles
466 retrieved from the helicon wave dispersion relation, which is
467 thereafter derived accounting for the non-uniformity of the ex-
468 ternal magnetic field along z . This approach implicitly as-
469 sumes that the plasma production entirely relies on the wave-
470 mode power coupling. Although the helicon regime is not
471 proven here by direct measurement of the excited wave, previ-
472 ous experiments performed on the same device operated with
473 similar ranges of magnetic field strength and input power have
474 shown the presence of the propagating wave¹¹. Considering
475 that the electric $\tilde{\mathbf{E}}$ and magnetic $\tilde{\mathbf{B}}$ components of the exited
476 wave are described^{47,48} as

$$477 \tilde{\mathbf{E}}, \tilde{\mathbf{B}} \sim \exp[i(m\theta + k_z z - \omega t)], \quad (1)$$

478 where m is the azimuthal mode number, θ is the azimuthal
479 angle and k_z is the axial wavenumber, Maxwell equations as-
480 sume the form

$$480 \nabla \cdot \tilde{\mathbf{B}} = 0, \quad (2a)$$

$$481 \nabla \times \tilde{\mathbf{E}} = i\omega\tilde{\mathbf{B}}, \quad (2b)$$

$$482 \nabla \times \tilde{\mathbf{B}} = \mu_0\mathbf{j}. \quad (2c)$$

483 The electron momentum equation is written as

$$484 -en_p\tilde{\mathbf{E}} = i\frac{m_e}{e}\mathbf{j}_e(\omega + i\nu) - \mathbf{j}_e \times \mathbf{B}, \quad (3)$$

485 where \mathbf{j}_e is the electron current density, \mathbf{B} is the external mag-
486 netic field and ν is a collision rate accounting for all dissipa-
487 tion phenomena. Additional comments and derivation of
488 Equation 3 are reported in⁴⁷. The widespread ideal assump-
489 tion of perfectly uniform magnetic field is not appropriate in
490 the actual case. Therefore, although still simplistic, it is as-
491 sumed that $\mathbf{B} = B(z)\hat{\mathbf{z}}$, i.e. only the variation of the magnetic

TABLE II. Helicon wave parameters at $z = 10$ cm.

	Conf. A	Conf. B	Conf. C	Conf. D	Conf. E
r_p [cm]	7.3	8.1	5.1	4.0	3.5
k_z [cm ⁻¹]	0.26	0.26	0.26	0.26	0.26
λ_z [cm]	24	24	24	24	24
κ_1 [cm ⁻¹]	0.46	0.41	0.68	0.88	1.03
κ_2 [cm ⁻¹]	0.14	0.17	0.07	-0.01	-0.08

490 field along z is accounted for. Combining Equation 2a-(2c)
491 and Equation 3, one obtains

$$\left(\frac{\omega + i\nu}{\omega_{ce}}\right) \nabla \times (\nabla \times \tilde{\mathbf{B}}) + k_z \nabla \times \tilde{\mathbf{B}} + \frac{\mu_0 \omega en_p}{B} \tilde{\mathbf{B}} = \mathbf{0}, \quad (4)$$

492 where the explicit dependence on z has been omitted, ω_{ce} is
493 the electron cyclotron frequency and the rest is conventional.
494 Detailed derivation of Equation 4 is likewise included in⁴⁷.
495 Eventually, in the limit of $m_e \rightarrow 0$, the local dispersion relation
496 is retrieved in the same shape of the well known 0D dispersion
497 relation, i.e.

$$k(z)k_z = \frac{\mu_0 \omega en_p(z)}{B(z)}, \quad (5)$$

498 where $k(z)$ indicates the total wavenumber. The wave bound-
499 ary conditions are fixed by⁴⁸

$$mk(z)J_m[k_r(z)r_p(z)] + k_z J'_m[k_r(z)r_p(z)] = 0, \quad (6)$$

500 where J_m and J'_m are the Bessel function of the first kind
501 of order m and its derivative, respectively, $k_r(z)$ is the lo-
502 cal radial wavenumber and $r_p(z)$ is the local plasma ra-
503 dius. The value of k_z is fixed by the antenna length,
504 i.e. $k_z = \pi/d_A, 3\pi/d_A, 5\pi/d_A$, etc. Pretending that only the
505 first order axial mode is coupled with the antenna, the compu-
506 tation algorithm includes:

- 507 • the axial wavenumber is estimated as $k_z = \pi/d_A$, there-
508 fore the axial wavelength is $\lambda_z = 24$ cm;
- 509 • $r_p(z)$ is set equal to the radius of the magnetic stream-
510 line crossing the tube edge at $z = 0$, see Figure 2;
- 511 • considering the geometry of the antenna and the direc-
512 tion of the external magnetic field, it is imposed that
513 $m = +1$;
- 514 • two cases are distinguished:
 - 515 1. $k_r(z)$ is computed numerically from Equation 6
516 and it is named as $\kappa_1(z)$ for the sake of clarity in
517 the following;
 - 518 2. $k_r(z)$ is evaluated as $\kappa_1(z) \sin[\alpha(z)]$ referred to as
519 $\kappa_2(z)$ hereafter. Here $\alpha(z)$ is the local magnetic
520 field divergence angle. The purpose of this heuris-
521 tic strategy is to provide the model with the in-
522 formation that the applied magnetic field is not

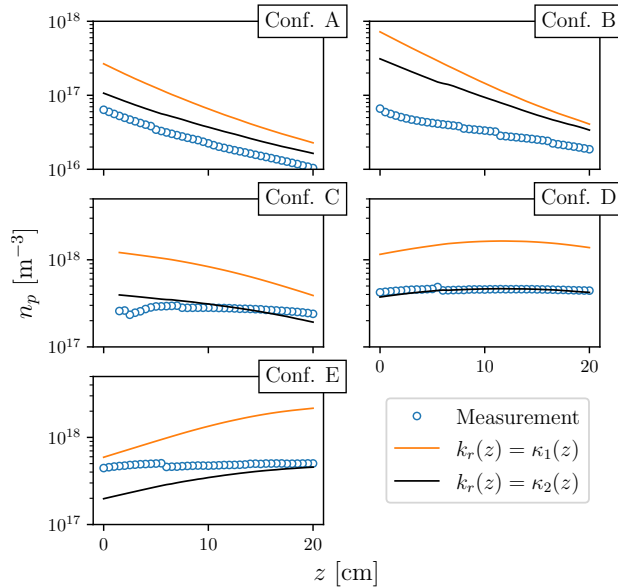


FIG. 14. Plasma density at $r = 0$ computed using the helicon waves dispersion relation in the $k_r(z) = \kappa_1(z)$ and $k_r(z) = \kappa_2(z)$ cases compared to measurement data.

523 purely axial. In doing so, it is postulated that
 524 the helicon wave resonance cone reduces to a line
 525 at the magnetic throat, i.e. where $\alpha = 0$, thus k
 526 equals k_z .

- 527 • the profile $n_p(z)$ is consequently computed from Equa-
 528 tion 5 for the aforementioned two cases.

529 Numerical values of the relevant parameters are reported
 530 in Table II for all magnetic configurations. In Figure 14, the
 531 obtained theoretical curves are compared with measurements
 532 of n_p extracted from Figure 9 at $x, y = 0$ for all the tested
 533 magnetic configurations. In general, it is found that the case
 534 $k_r(z) = \kappa_1(z)$ provides an overestimation of the plasma den-
 535 sity. When dealing with Conf.s D and E, the $k_r(z) = \kappa_2(z)$ case
 536 is in very good agreement with the data in correspondence
 537 of the magnetic throat, that is where the strong assumption
 538 $\mathbf{B} = B(z)\hat{\mathbf{z}}$ is more representative. Ultimately, n_p measured in
 539 Conf. C is in relatively good agreement with the latter case.
 540 It is noted that even the $k_r(z) = \kappa_2(z)$ case overestimates the
 541 measured values of n_p for Conf.s A and B, although match-
 542 ing the qualitative profile. This suggests that the helicon wave
 543 is evanescent in this region of the plasma since the measured
 544 n_p is lower than the one required by the dispersion relation.
 545 In conclusion, these profiles of n_p computed from the disper-
 546 sion relation represent a first effective estimation of the actual
 547 spatial evolution of plasma density. Therefore, these quanti-
 548 tative information can be of some convenience for guessing
 549 the propagation region of helicon waves and for preliminary
 550 modeling of the plasma dynamics and/or design of the axial
 551 magnetic field profile.

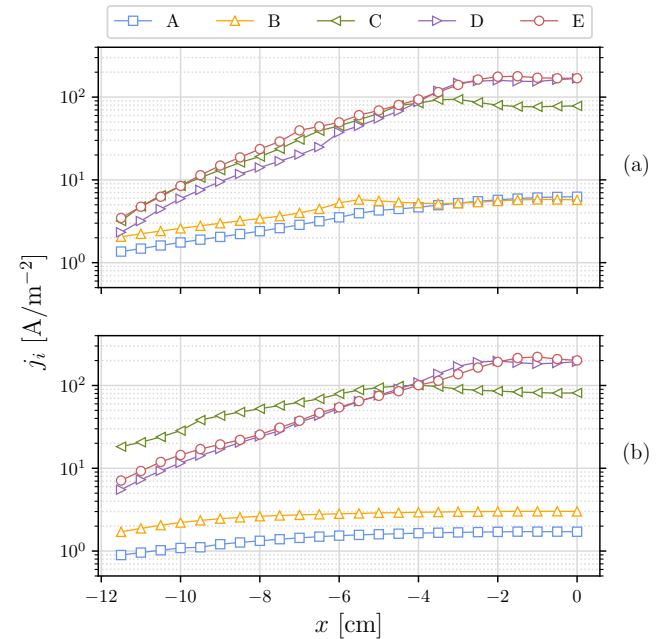


FIG. 15. Ion current density at (a) $z = 5$ and (b) $z = 15$ cm for the five magnetic configurations.

TABLE III. Plume divergence parameter δ from data in Figure 15.

	Conf. A	Conf. B	Conf. C	Conf. D	Conf. E
δ at $z = 5$ cm	0.218	0.359	0.041	0.014	0.021
δ at $z = 15$ cm	0.523	0.567	0.224	0.028	0.035

552 D. PPGR measurements

553 A further insight into the properties of the plasma when
 554 operating with the different magnetic topologies is ren-
 555 dered by the employment of the PPGR described in Sec-
 556 tion III. The probe is displaced radially along the x axis
 557 at $z = 5$ cm and $z = 15$ cm in order to analyze the diver-
 558 gence of the extracted plasma plume. The measurements of
 559 j_i are shown in Figure 15(a-b). Table III gathers the val-
 560 ues of the divergence parameter δ computed as the ratio
 561 $j_i(x = -11.5 \text{ cm}) / j_i(x = 0 \text{ cm})$. Results confirm that a low-
 562 current high-divergence ion beam is extracted from the HP
 563 source when operating in Conf. A and B. Differently, the ion
 564 beams related to Conf.s C, D and E feature a similar low-
 565 divergence profile of j_i in the proximity of the tube exit, see
 566 Figure 15(a). Yet, the divergence angle of Conf. C rapidly
 567 grows as the plasma expands downstream, cf. Figure 15(b).
 568 The highest value of j_i is recorded in Conf. E at $z = 15$ cm,
 569 in agreement with the largest n_p probed in the same configu-
 570 ration. Larger values of j_i relate well with higher propellant
 571 utilization efficiency, which is a desirable working condition
 572 for space propulsion applications.

TABLE IV. Order of magnitude of relevant velocity quantities.

	$\mathcal{O}(v)$
Ion acoustic velocity	$v_B = \sqrt{kT_e/m_i} \approx 2000 \text{ ms}^{-1}$
Thermal velocity	$v_{th} = \sqrt{8kT_i/\pi m_i} \approx 275 \text{ ms}^{-1}$

573 E. LIF measurements

574 Using LIF spectroscopy, the velocity distribution functions
 575 of krypton atoms Kr I and ions Kr II are inferred. Informa-
 576 tion about the velocity of the ions is of particular inter-
 577 est for driving conclusions about propulsive performance. On
 578 the other hand, knowledge of the atoms velocity is useful for
 579 modeling of the plasma flow. Table IV exemplifies the order
 580 of magnitude of the relevant velocity terms in the HP
 581 source operating with Kr. Radial profiles of Kr I VDF are
 582 evaluated at $z = 12 \text{ cm}$ and shown in Figure 16 for all mag-
 583 netic configurations. The spatial resolution is 10 mm. In this
 584 case, the reported data did not require any post-processing as
 585 a adequate signal-to-noise ratio was found. These measure-
 586 ments show that the most probable velocity of Kr I is nearly
 587 unchanged over the different magnetic topologies, reading
 588 $\sim 250 \div 300 \text{ ms}^{-1}$, therefore in the order of the thermal ve-
 589 locity assuming $T_i \approx 300 \text{ K}$, cf. Table IV. No dependence of
 590 the velocity on the radial location y is recorded. Dissimilar
 591 values of velocity spread are found between the magnetic con-
 592 figurations, with a broader VDF for Conf. C and Conf. D.

593 Axial VDFs of Kr II are probed in the same radial region
 594 with a spatial resolution of 5 mm at three distinct axial posi-
 595 tions, i.e. $z = 10.5 \text{ cm}$, $z = 12 \text{ cm}$ and $z = 25 \text{ cm}$. At some
 596 y locations, the LIF signal was not distinguishable from the
 597 background noise due to small local values of n_p , therefore
 598 mapping of the VDFs was not possible. For the very same
 599 reason, Conf.s A and B did not allow obtaining an appropriate
 600 signal-to-noise ratio in any of the probed locations. Raw
 601 VDFs are post-processed using a least squares Gaussian fit.
 602 The resulting profiles when the HP source operates in Conf.s
 603 C, D and E are reported in Figure 17, 18 and 19, respectively.
 604 In addition, the most probable velocity is extracted and plot
 605 in Figure 20 thus to facilitate comparison among the various
 606 magnetic configurations. It is noticed that the profiles related
 607 to Conf.s C and D feature a nearly identical trend, whereas the
 608 ion velocity in Conf. E generally retains lower readings. This
 609 is in agreement with the measured values of V_p which remain
 610 below those concerning Conf. C and D, cf. Figure 11. In the
 611 further upstream regions, namely $z = 10.5 \text{ cm}$ and $z = 12 \text{ cm}$,
 612 velocities smaller than $\sim 250 \text{ ms}^{-1}$ are measured, therefore in
 613 the order of the thermal velocity assuming $T_i \approx 300 \text{ K}$. Con-
 614 versely, at $z = 25 \text{ cm}$, all the velocities increase by a factor of
 615 2 to 3, reaching values as high as $\sim 500 \text{ ms}^{-1}$. These small
 616 velocities somewhat concur with the fact that the magnetic
 617 field is weakly divergent in the probed region for Conf.s C and
 618 D, while $z = 25 \text{ cm}$ represents the throat location for Conf. E.
 619 A weakly divergent magnetic field does not allow for a signifi-
 620 cant momentum gain imparted by the Lorentz force. Measure-
 621 ments farther downstream were prevented due to the limited

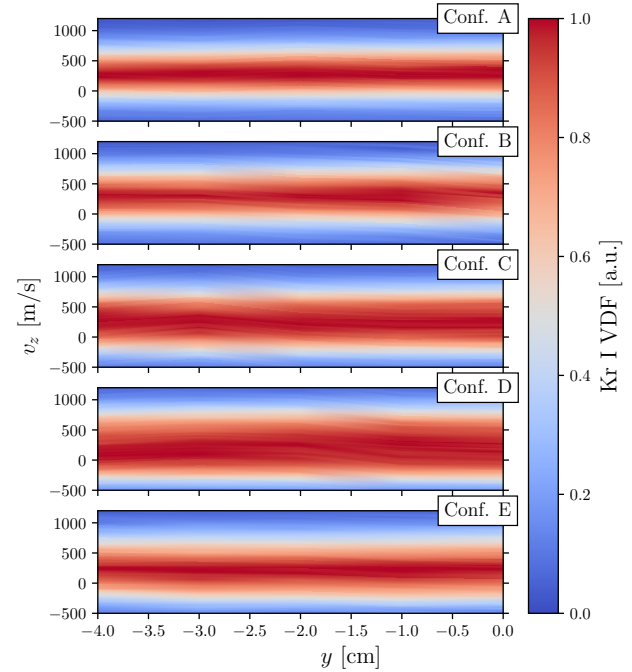


FIG. 16. Kr I velocity distribution function for the five magnetic configurations measured along the y axis at $z = 12 \text{ cm}$.

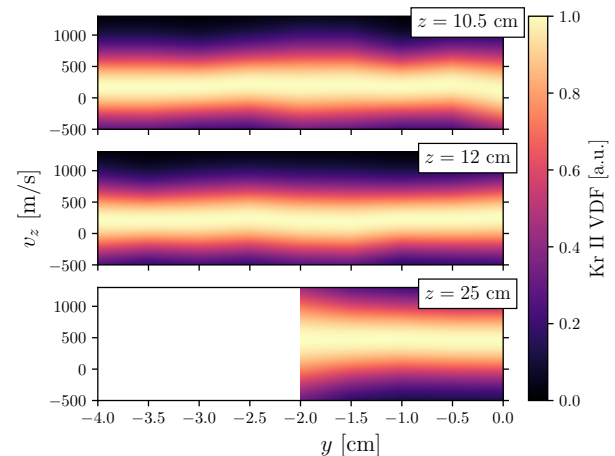


FIG. 17. Kr II velocity distribution function for Conf. C measured along the y axis at $z = 10.5, 12$ and 25 cm .

622 size of the vacuum chamber. Similar small values of ion ve-
 623 locity are reported in Ref. 49 using LIF on a large scale HP
 624 source. In all of the magnetic configurations, the drop of V_p
 625 is fairly small (in the order of 1 V) within $z < 21 \text{ cm}$, cf. Fig-
 626 ure 11. Considering Conf. E for instance, since at $z < 25 \text{ cm}$
 627 the magnetic field is convergent, it is expected that the favored
 628 inward transport of electrons do not allow for a significant po-
 629 tential drop in this region. In the purely electrostatic case,

This is the author's peer reviewed, accepted manuscript. However, the online version of record will be different from this version once it has been copyedited and typeset.
PLEASE CITE THIS ARTICLE AS DOI: 10.1063/5.0069983

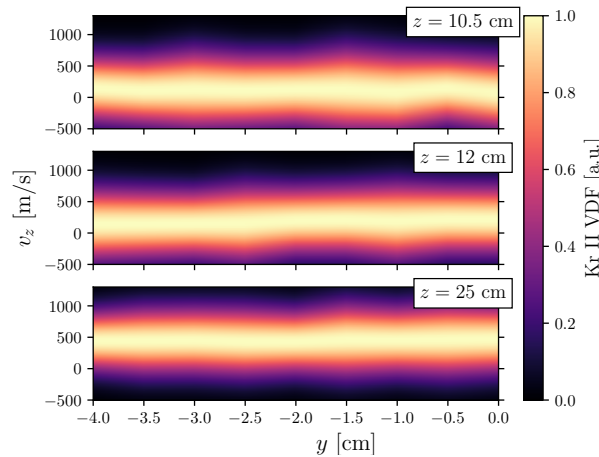


FIG. 18. Kr II velocity distribution function for Conf. D measured along the y axis at $z = 10.5, 12$ and 25 cm.

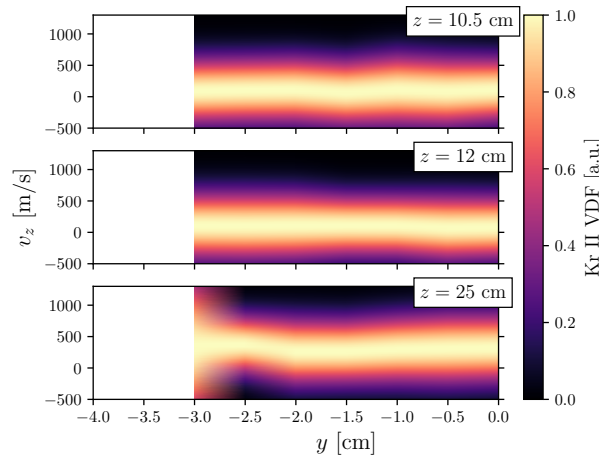


FIG. 19. Kr II velocity distribution function for Conf. E measured along the y axis at $z = 10.5, 12$ and 25 cm.

630 a potential drop of ~ 1 V translates into an ion velocity in-
631 crease of ~ 1.5 km s $^{-1}$. Hence, the acceleration of the ions
632 throughout the MN does not fully exploit the available en-
633 ergy. This phenomenon is related to some dissipation phe-
634 nomenon, e.g. collisions, as later discussed. Moreover, al-
635 though no sonic condition is achieved at the magnetic throat
636 in Conf.s C and D, ions experience a further acceleration in
637 the divergent part of the nozzle, see Figure 20. It suggests that
638 the sonic point, if ever reached, is shifted downstream, in con-
639 trast with the ideal postulation of gas-dynamics-like plasma
640 expansion⁵⁰. In this experiment, the ions might reach the
641 sonic speed only at the sheath edge that forms downstream
642 between the chamber wall and the plasma plume. Numer-
643 ous works focusing on modeling of magnetic nozzle dynam-
644 ics have assumed that the ion Mach number equals unity at
645 the throat⁵¹⁻⁵³. Albeit this condition conveniently allows sep-
646 arating the processes of plasma generation and plasma accel-

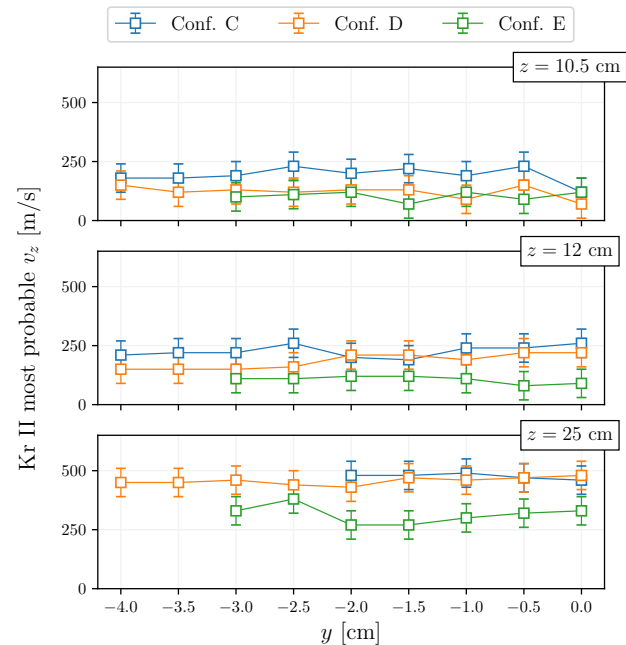


FIG. 20. Kr II most probable axial velocity extracted from Figure 17-19. Error bar is 60 m s $^{-1}$ (typical instrument absolute error).

647 eration, it is not representative in this case as well as in some
648 other plasma beams^{24,54}. Collard *et al*²⁴ have examined a list
649 of phenomena which are potentially responsible for separation
650 of the magnetic throat and the sonic point, namely electron-
651 neutral collisions, charge-exchange collisions and ionization
652 within the plume. In the device herein analyzed, a combina-
653 tion of several dissipative phenomena is likely to contribute in
654 introducing a drag force term that prevents the ions to reach
655 the sonic speed. In Conf. C, for instance, a significant level
656 of ionization is localized in the near-field plume downstream
657 the magnetic throat, as previously noted when commenting on
658 Figure 9. This suggests that the energy stored in the electrons
659 is spent for ions generation rather than acceleration.

660 A parametric evaluation of the Kr II axial VDF is addition-
661 ally performed at $z = 25$ cm for the purpose of better grasping
662 the mechanisms occurring within the nozzle. The exploited
663 parameters are: input power (750 W and 900 W); mass flow
664 rate (0.5 mg s $^{-1}$, 1 mg s $^{-1}$ and 2 mg s $^{-1}$); current in the elec-
665 tromagnets (6 A and 8 A). The magnetic configuration is fixed
666 to Conf. D for this experiment because of its divergent shape
667 at $z = 25$ cm and larger signal-to-noise ratio with respect to
668 Conf. C. The resulting VDFs are shown in Figure 21, which
669 includes the raw data, the Gaussian fittings and the unfold
670 most probable velocities obtained at each working condition.
671 The overall tendency results clear. Indeed, higher ion veloci-
672 ties are attained as the mass flow rate decreases and the mag-
673 netic field is increased, whereas slower ions are recorded with
674 larger mass flow rates. These outcomes suggest that collisions
675 resulting from a larger pressure do play a role in the accelera-
676 tion process. At lower pressures, a larger mean free path is
677 expected, therefore allowing for greater values of T_e .

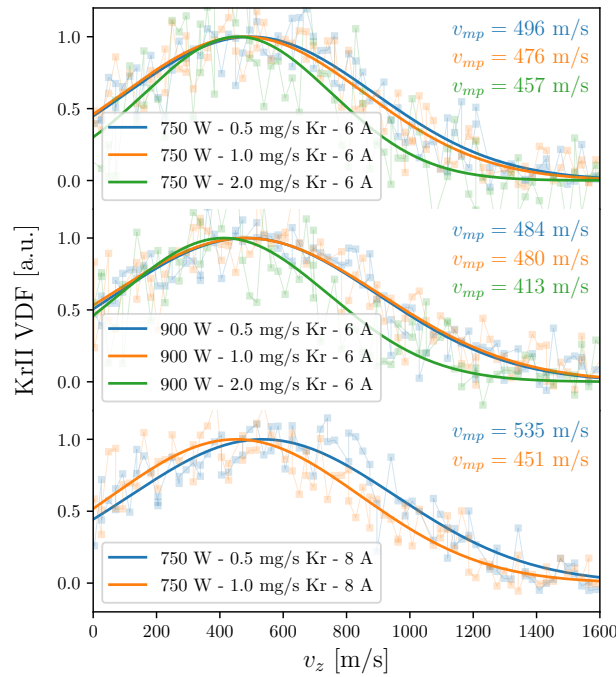


FIG. 21. Kr II axial VDF for Conf. D at $z = 25$ cm as function of P_{IN} , \dot{m} and electromagnets current. Scatter points indicate raw data, solid lines exemplify least squares Gaussian fittings.

678 V. CONCLUSION

679 In summary, several plasma properties are inferred via di-
 680 rect measurement to establish empirical approaches to thruster
 681 design and optimization. The magnetic throat is displaced
 682 along the reactor axis and the resultant plasma is studied in
 683 the near-field plume using electrostatic diagnostics and LIF
 684 spectroscopy. It is found that a low-current high-divergence
 685 plume is extracted from the plasma source when the magnetic
 686 throat is located upstream or in correspondence of the antenna
 687 center point. Plasma density measurements at the back plate
 688 emphasize that, in those cases, the generated plasma mainly
 689 remains within the discharge tube and is lost at the radial and
 690 back boundaries. Larger ion currents and higher confinement
 691 levels are attained when the magnetic throat is located down-
 692 stream the antenna, namely at a distance at least equal to the
 693 wavelength corresponding to the first order axial mode of the
 694 helicon wave. Hence, optimization of the plasma generation
 695 process in a Helicon thruster would include the separation of
 696 the magnetic throat from the antenna location in accordance
 697 with the excited helicon wavelength.

698 Theoretical axial profiles for the plasma density are directly
 699 derived from the dispersion relation under the hypothesis of
 700 non-uniform magnetic field. Comparison with probe mea-
 701 surements show relatively good agreement therefore hinting
 702 the applicability of this theoretical description for guessing

703 the helicon wave propagation region. Furthermore, prelim-
 704 inary modeling and design of Helicon thrusters can perhaps
 705 make use of this approach to shape the axial magnetic field
 706 profile.

707 The measured ion axial velocities exhibit small values, be-
 708 ing below the sonic condition at the magnetic throat. By mea-
 709 suring the most probable ion velocity obtained under differ-
 710 ent working parameters (input power, magnetic strength and
 711 mass flow rate), it is concluded that ionization and collisions
 712 occurring in the near-field plume contribute to limiting the ion
 713 acceleration process.

714 ACKNOWLEDGMENTS

715 This project has received funding from the European
 716 Union's Horizon 2020 research and innovation program un-
 717 der grant agreement No 870542 (HelIcon Plasma Thruster
 718 for In-space Applications).

719 CONFLICT OF INTEREST

720 The authors have no conflicts to disclose.

721 DATA AVAILABILITY

722 The data that support the findings of this study are available
 723 from the corresponding author upon reasonable request.

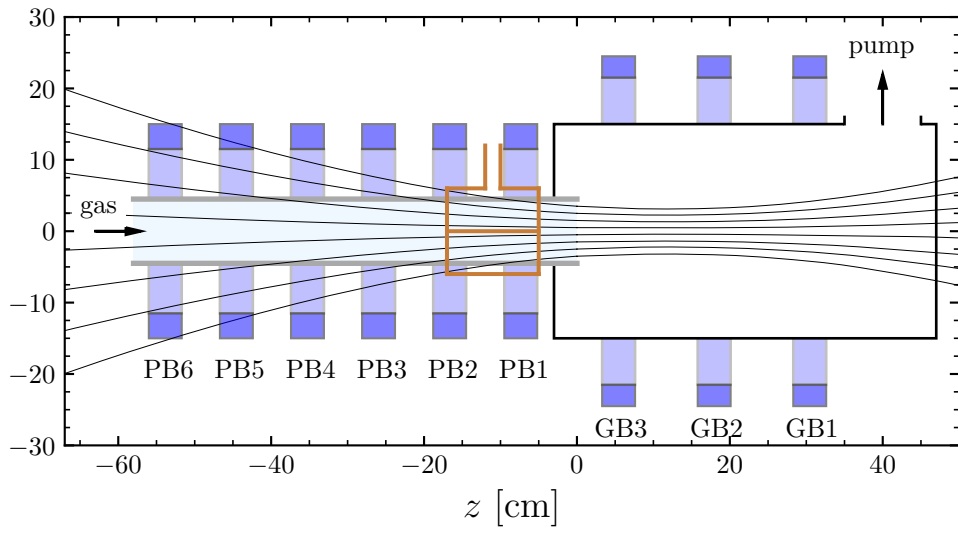
724 REFERENCES

- 725 ¹Igor Levchenko, Kateryna Bazaka, Yongjie Ding, Yevgeny Raitses,
 726 Stéphane Mazouffre, Torsten Henning, Peter J. Klar, Shunjiro Shinohara,
 727 Jochen Schein, Laurent Garrigues, Minkwan Kim, Dan Lev, Francesco Tac-
 728 cogna, Rod W. Boswell, Christine Charles, Hiroyuki Koizumi, Yan Shen,
 729 Carsten Scharlemann, Michael Keidar, and Shuyan Xu. Space micropropul-
 730 sion systems for Cubesats and small satellites: From proximate targets to
 731 furthestmost frontiers. *Applied Physics Reviews*, 5(1), 2018.
- 732 ²Javier Martínez Martínez, Dmytro Rafalskyi, and Ane Aanesland. Devel-
 733 opment and Testing of the NPT30-I2 Iodine Ion Thruster. In *36th Interna-*
 734 *tional Electric Propulsion Conference*, 2019.
- 735 ³Antonio Gurciullo, Julien Jarrige, Paul Lascombes, and Denis Packan. Ex-
 736 perimental performance and plume characterisation of a miniaturised 50W
 737 Hall thruster. In *36th International Electric Propulsion Conference*, 2019.
- 738 ⁴I. Levchenko, S. Xu, S. Mazouffre, D. Lev, D. Pedrini, D. Goebel, L. Gar-
 739 rrigues, F. Taccogna, and K. Bazaka. Perspectives, frontiers, and new hori-
 740 zons for plasma-based space electric propulsion. *Physics of Plasmas*, 27(2),
 741 2020.
- 742 ⁵E. Dale, B. Jorns, and A. Gallimore. Future Directions for Electric Propul-
 743 sion Research. *Aerospace*, 7(120), 2020.
- 744 ⁶David Krejci, Lou Grimaud, Tony Schönherr, Valentin Hugonnaud,
 745 Alexander Reissner, and Bernhard Seifert. ENPULSION NANO and MI-
 746 CRO propulsion systems: development and testing. In *AIAA Propulsion*
 747 *and Energy Forum*, 2021.
- 748 ⁷Dillon O'reilly, Georg Herdrich, and Darren F. Kavanagh. Electric propul-
 749 sion methods for small satellites: A review. *Aerospace*, 8(1):1–30, 2021.
- 750 ⁸S. N. Bathgate, M. M.M. Bilek, and D. R. McKenzie. Electrodeless plasma
 751 thrusters for spacecraft: A review. *Plasma Science and Technology*, 19(8),
 752 2017.

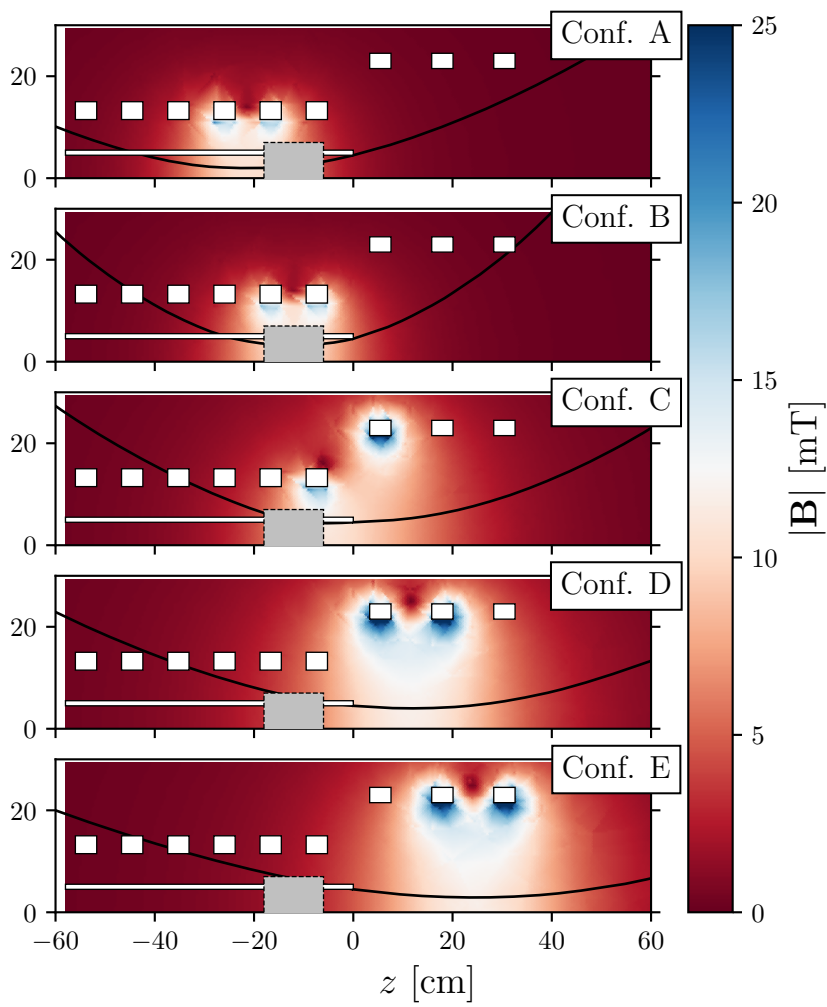
This is the author's peer reviewed, accepted manuscript. However, the online version of record will be different from this version once it has been copyedited and typeset.
PLEASE CITE THIS ARTICLE AS DOI: 10.1063/5.0069983

- 753 ⁹Shunjiro Shinohara. Helicon high-density plasma sources: Physics and
754 applications. *Advances in Physics: X*, 3(1):185–220, 2018.
- 755 ¹⁰K. Takahashi. Helicon-type radiofrequency plasma thrusters and magnetic
756 plasma nozzles. In *Reviews of Modern Plasma Physics*, volume 3. Springer
757 Singapore, 2019.
- 758 ¹¹Alfio E Vinci and Stéphane Mazouffre. Direct experimental comparison of
759 krypton and xenon discharge properties in the magnetic nozzle of a helicon
760 plasma source. *Physics of Plasmas*, 28(033504), 2021.
- 761 ¹²Kazunori Takahashi. Magnetic nozzle radiofrequency plasma thruster ap-
762 proaching twenty percent thruster efficiency. *Scientific Reports*, 11(1):1–12,
763 2021.
- 764 ¹³Nicolas Bellomo, Mirko Magarotto, Marco Manente, Fabio Trezzolani,
765 Riccardo Mantellato, Lorenzo Cappellini, Devis Paulon, Antonio Selmo,
766 Davide Scalzi, Marco Minute, Matteo Duzzi, Alessandro Barbato, Alessan-
767 dro Schiavon, Simone Di Fede, Nabil Souhair, Paola De Carlo, Francesco
768 Barato, Fabiana Milza, Elena Toson, and Daniele Pavarin. Design and In-
769 orbit Demonstration of REGULUS, an Iodine electric propulsion system.
770 *CEAS Space Journal*, (0123456789), 2021.
- 771 ¹⁴Seth J Thompson, Fort Collins, Casey C Farnell, Shawn C Farnell, Plasma
772 Controls, Fort Collins, Desiree D Williams, John P Chandler, Fort Collins,
773 John D Williams, and Fort Collins. Evaluation of Iodine Compatible Cath-
774 ode Configurations. *36th International Electric Propulsion Conference*,
775 pages 1–21, 2019.
- 776 ¹⁵M. Light, I. D. Sudit, F. F. Chen, and D. Arnush. Axial propagation of
777 helicon waves. *Physics of Plasmas*, 2(11):4094–4103, 1995.
- 778 ¹⁶D. D. Blackwell, T. G. Madziwa, D. Arnush, and F. F. Chen. Evidence for
779 Trivelpiece-Gould Modes in a Helicon Discharge. *Physical Review Letters*,
780 88(14):4, 2002.
- 781 ¹⁷K. Takahashi, T. Lafleur, C. Charles, P. Alexander, R. W. Boswell, M. Per-
782 ren, R. Laine, S. Pottinger, V. Lappas, T. Harle, and D. Lamprou. Direct
783 thrust measurement of a permanent magnet helicon double layer thruster.
784 *Applied Physics Letters*, 98(14):2–4, 2011.
- 785 ¹⁸L. T. Williams and M. L.R. Walker. Thrust measurements of a helicon
786 plasma source. *47th AIAA/ASME/SAE/ASEE Joint Propulsion Conference*
787 *and Exhibit 2011*, pages 1–15, 2011.
- 788 ¹⁹S. Pottinger, V. Lappas, C. Charles, and R. Boswell. Performance character-
789 ization of a helicon double layer thruster using direct thrust measurements.
790 *Journal of Physics D: Applied Physics*, 44(23), 2011.
- 791 ²⁰K. Takahashi, C. Charles, R. Boswell, and A. Ando. Performance improve-
792 ment of a permanent magnet helicon plasma thruster. *Journal of Physics*
793 *D: Applied Physics*, 46(35), 2013.
- 794 ²¹Kazunori Takahashi, Yoshinori Takao, and Akira Ando. Thrust imparted
795 by a stepped-diameter magnetic nozzle rf plasma thruster. *Applied Physics*
796 *Letters*, 113(3), 2018.
- 797 ²²J. Navarro-Cavallé, M. Wijnen, P. Fajardo, and E. Ahedo. Experimental
798 characterization of a 1 kW Helicon Plasma Thruster. *Vacuum*, 149:69–73,
799 2018.
- 800 ²³J. Navarro-Cavallé, M. Wijnen, P. Fajardo, E. Ahedo, V. Gomez,
801 A. Giménez, and Mercedes Ruiz. Development and Characterization of
802 the Helicon Plasma Thruster Prototype HPT05M. In *36th International*
803 *Electric Propulsion Conference*, number September, 2019.
- 804 ²⁴T. A. Collard and B. A. Jorns. Magnetic nozzle efficiency in a low power
805 inductive plasma source. *Plasma Sources Science and Technology*, 28(10),
806 2019.
- 807 ²⁵Eduardo Ahedo and Jaime Navarro-Cavallé. Helicon thruster plasma
808 modeling: Two-dimensional fluid-dynamics and propulsive performances.
809 *Physics of Plasmas*, 20(4), 2013.
- 810 ²⁶T. Lafleur. Helicon plasma thruster discharge model. *Physics of Plasmas*,
811 21(4), 2014.
- 812 ²⁷M. Magarotto, D. Melazzi, and D. Pavarin. Study on the influence of
813 the magnetic field geometry on the power deposition in a helicon plasma
814 source. *Journal of Plasma Physics*, 85(4):1–19, 2019.
- 815 ²⁸K. Takahashi, Y. Takao, and A. Ando. Increased Thrust-to-Power Ratio
816 of a Stepped-Diameter Helicon Plasma Thruster with Krypton Propellant.
817 *Journal of Propulsion and Power*, 2020.
- 818 ²⁹J. M. Little and E. Y. Choueri. Electron Cooling in a Magnetically Expand-
819 ing Plasma. *Physical Review Letters*, 117(22):1–5, 2016.
- 820 ³⁰T. Lafleur, C. Charles, and R. W. Boswell. Characterization of a helicon
821 plasma source in low diverging magnetic fields. *Journal of Physics D:*
822 *Applied Physics*, 44(5), 2011.
- 823 ³¹Alexander Bennet, Christine Charles, and Rod Boswell. Non-local plasma
824 generation in a magnetic nozzle. *Physics of Plasmas*, 26(7), 2019.
- 825 ³²I. D. Sudit and F. F. Chen. RF Compensated Probes for High-density Dis-
826 charges. *Plasma Sources Science and Technology*, 3(2):162–168, 1994.
- 827 ³³F. F. Chen. Lectures Notes on Langmuir Probe Diagnostics, 2003.
- 828 ³⁴F. F. Chen. Langmuir probes in RF plasma: Surprising validity of OML
829 theory. *Plasma Sources Science and Technology*, 18(3), 2009.
- 830 ³⁵F. F. Chen. Langmuir probe analysis for high density plasmas. *Physics of*
831 *Plasmas*, 8(6):3029–3041, 2001.
- 832 ³⁶S. Mazouffre, G. Largeau, L. Garrigues, C. Boniface, and K. Dannenmayer.
833 Evaluation of various probe designs for measuring the ion current density in
834 a Hall thruster plume. *35th International Electric Propulsion Conference*,
835 (8-12 October):IEPC–2017–336, 2017.
- 836 ³⁷S. Mazouffre. Mesure de la densité de courant ionique dans le jet plasma
837 d’un propulseur de Hall. Théorie et instrumentation. Technical report, 2016.
- 838 ³⁸S. Mazouffre. Laser-induced fluorescence diagnostics of the cross-field dis-
839 charge of Hall thrusters. *Plasma Sources Science and Technology*, 22(1),
840 2012.
- 841 ³⁹A. Lejeune, G. Bourgeois, and S. Mazouffre. Kr II and Xe II axial velocity
842 distribution functions in a cross-field ion source. *Physics of Plasmas*, 19(7),
843 2012.
- 844 ⁴⁰A. Kramida, Yu. Ralchenko, J. Reade, and Team NIST ASD. NIST
845 Atomic Spectra Database (ver. 5.8), [Online]. Available:
846 <https://physics.nist.gov/asd> [2021, June 7]. National Institute of Stan-
847 dards and Technology, Gaithersburg, MD, 2020.
- 848 ⁴¹V. Kaufman. Wavelengths and Energy Levels of Neutral Kr⁸⁴ and Level
849 Shifts in All Kr Even Isotopes. *J. Res. Natl. Inst. Stand. Technol.*, 98, 1993.
- 850 ⁴²C. J. Humphreys and E. Paul Jr. Interferometric Observations in the Spectra
851 of ⁸⁶Kr. *J. Opt. Soc. Am.*, 60:200–205, 1970.
- 852 ⁴³M. Martinez-Sanchez, J. Navarro-Cavallé, and E. Ahedo. Electron cooling
853 and finite potential drop in a magnetized plasma expansion. *Physics of*
854 *Plasmas*, 22(5):1–12, 2015.
- 855 ⁴⁴K. Takahashi and A. Ando. Enhancement of axial momentum lost to the
856 radial wall by the upstream magnetic field in a helicon source. *Plasma*
857 *Physics and Controlled Fusion*, 59(5), 2017.
- 858 ⁴⁵I. D. Sudit and F. F. Chen. Discharge equilibrium of a helicon plasma.
859 *Plasma Sources Science and Technology*, 5(1):43–53, 1996.
- 860 ⁴⁶D. Bose, T. R. Govidan, and M. Meyyappan. Modeling of a helicon plasma
861 source. *IEEE TRANSACTIONS ON PLASMA SCIENCE*, 31(4), 2003.
- 862 ⁴⁷F. F. Chen and D. Arnush. Generalized theory of helicon waves. I. Normal
863 modes. *Physics of Plasmas*, 4(9):3411–3421, 1997.
- 864 ⁴⁸P. Chabert and N. Braithwaite. *Physics of Radio-Frequency Plasmas*. Cam-
865 bridge University Press, 2011.
- 866 ⁴⁹Yuriko TANIDA, Daisuke KUWAHARA, and Shunjiro SHINOHARA. Spatial
867 Profile of Ion Velocity Distribution Function in Helicon High-
868 Density Plasma by Laser Induced Fluorescence Method. *Transactions of*
869 *the Japan Society for Aeronautical and Space Sciences, Aerospace Tech-*
870 *nology Japan*, 14(ists30):Pb7 – Pb12, 2016.
- 871 ⁵⁰S. A. Andersen, V. O. Jensen, P. Nielsen, and N. D’Angelo. Continuous
872 supersonic plasma wind tunnel. *Physics of Fluids*, 12(3):557–560, 1969.
- 873 ⁵¹E. Ahedo and M. Merino. Two-dimensional supersonic plasma acceleration
874 in a magnetic nozzle. *Physics of Plasmas*, 17(7):1–15, 2010.
- 875 ⁵²M. Merino and E. Ahedo. Plasma detachment in a propulsive magnetic
876 nozzle via ion demagnetization. *Plasma Sources Science and Technology*,
877 23(3), 2014.
- 878 ⁵³E. Ahedo, S. Correyero, J. Navarro, and M. Merino. Macroscopic and para-
879 metric study of a kinetic plasma expansion in a paraxial magnetic nozzle.
880 *Plasma Sources Science and Technology*, 29(045017):0–20, 2020.
- 881 ⁵⁴Sara Correyero, Julien Jarrige, Denis Packan, and Eduardo Ahedo. Ion
882 acceleration in the magnetic nozzle of an ECR thruster: Comparison of ex-
883 perimental measurements with a quasi 1D kinetic model. *Space Propulsion*
884 *2018*, (May):1–8, 2018.

This is the author's peer reviewed, accepted manuscript. However, the online version of record will be different from this version once it has been copyedited and typeset.
PLEASE CITE THIS ARTICLE AS DOI: 10.1063/5.0069983

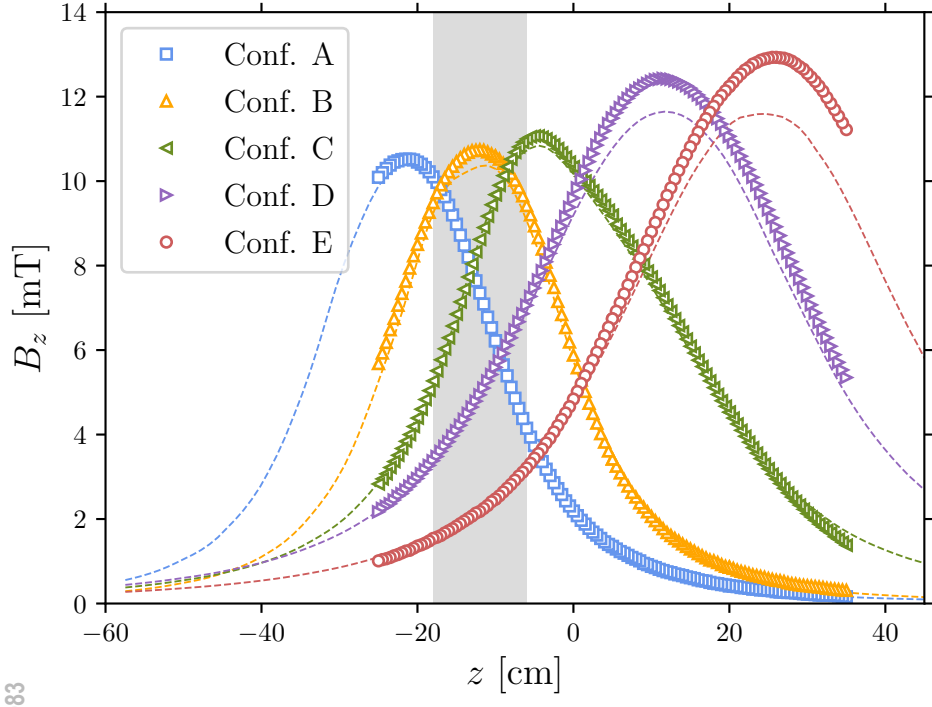


This is the author's peer reviewed, accepted manuscript. However, the online version of record will be different from this version since it has been copyedited and typeset.
PLEASE CITE THIS ARTICLE AS DOI: 10.1063/5.0069983



This is the author's peer reviewed, accepted manuscript. However, the online version of record will be different from this version once it has been copyedited and typeset.

PLEASE CITE THIS ARTICLE AS DOI: 10.1063/5.0069983

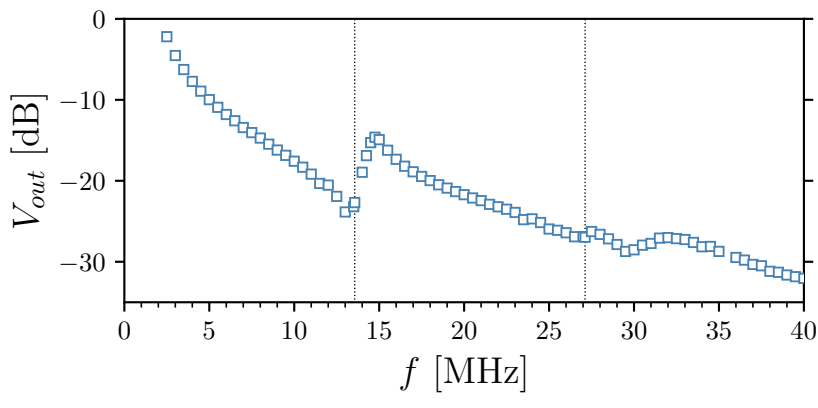


This is the author's peer reviewed, accepted manuscript. However, the online version of record will be different from this manuscript as it has been copyedited and typeset.

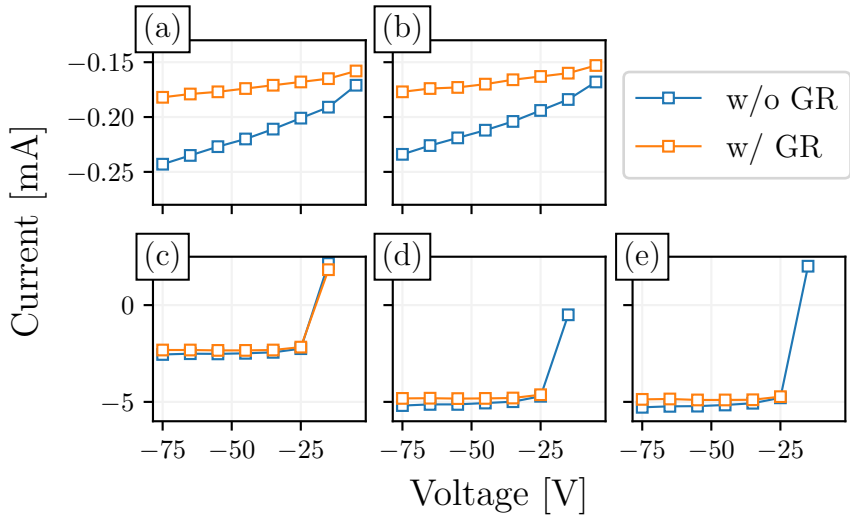
PLEASE CITE THIS ARTICLE AS DOI: 10.1063/1.5069983



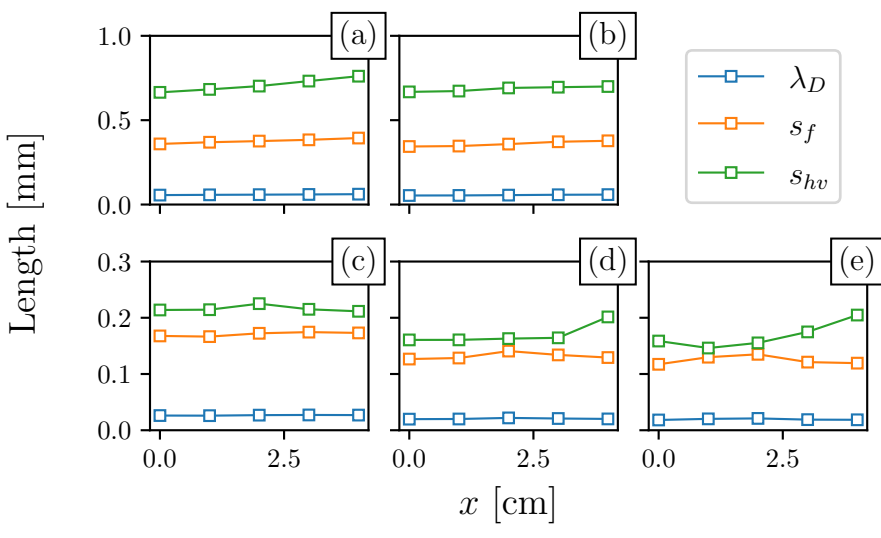
This is the author's peer reviewed, accepted manuscript. However, the online version of record will be different from this version once it has been copyedited and typeset.
PLEASE CITE THIS ARTICLE AS DOI: 10.1063/5.0069983



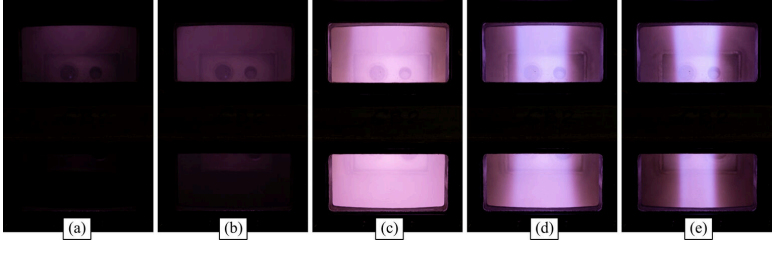
This is the author's peer reviewed, accepted manuscript. However, the online version of record will be different from this version once it has been copyedited and typeset.
PLEASE CITE THIS ARTICLE AS DOI: 10.1063/5.0069983



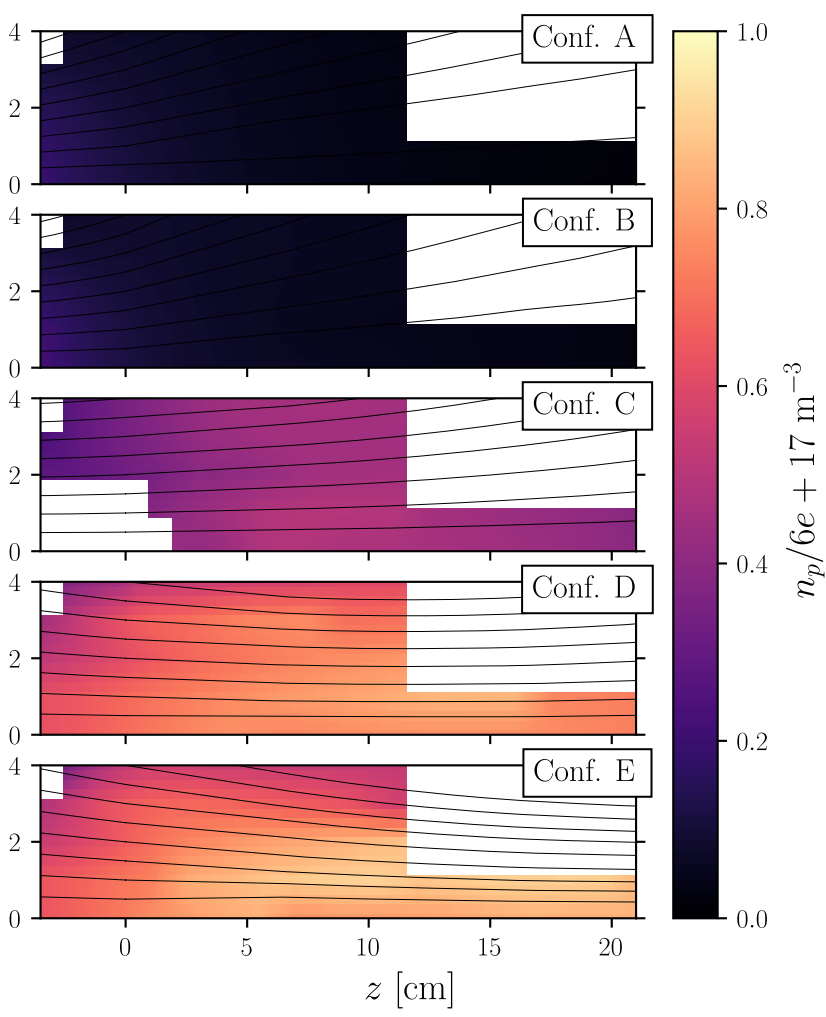
This is the author's peer reviewed, accepted manuscript. However, the online version of record will be different from this version once it has been copyedited and typeset.
PLEASE CITE THIS ARTICLE AS DOI: 10.1063/5.0069983



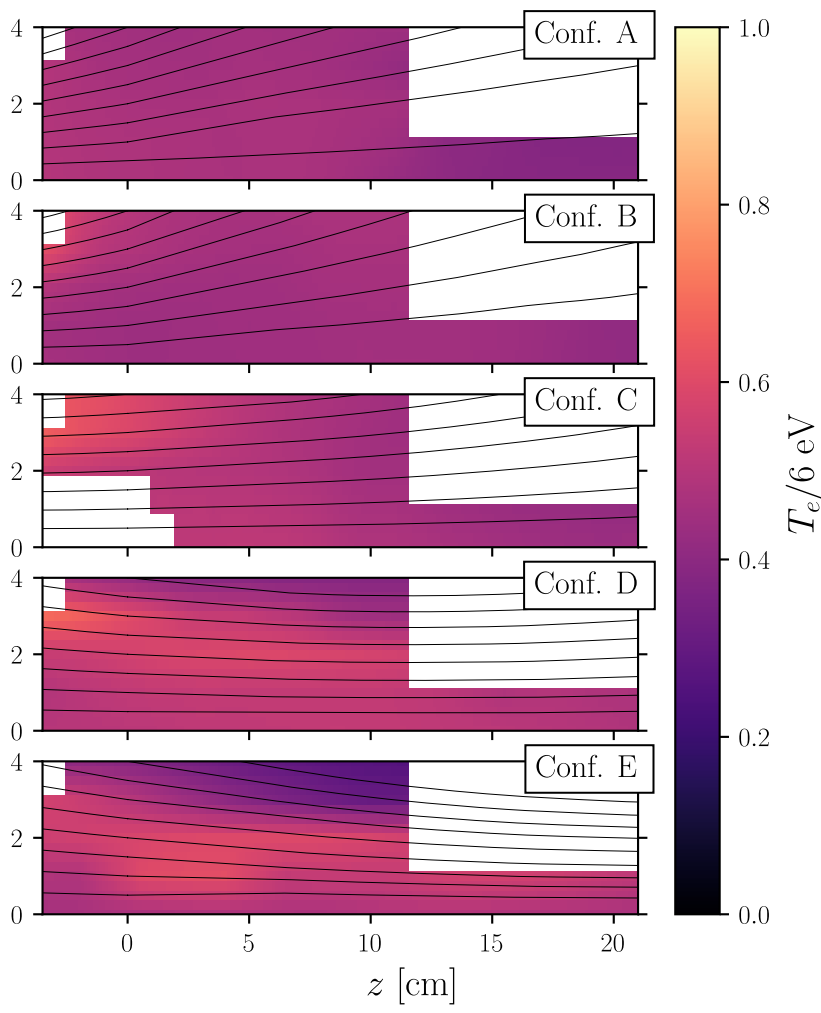
This is the author's peer reviewed, accepted manuscript. However, the online version of record will be different from this version once it has been copyedited and typeset.
PLEASE CITE THIS ARTICLE AS DOI: 10.1063/5.0069983



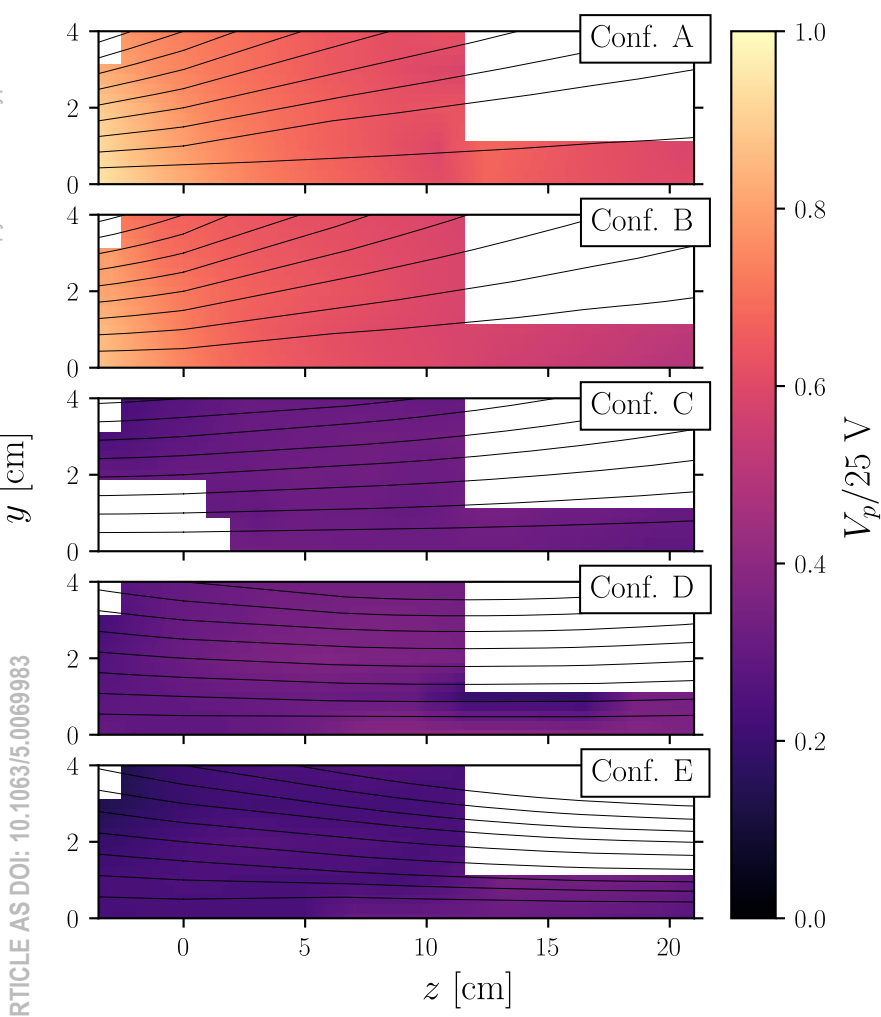
This is the author's peer reviewed, accepted manuscript. However, the online version of record will be different from this version once it has been copyedited and typeset.
PLEASE CITE THIS ARTICLE AS DOI: 10.1063/5.0069983



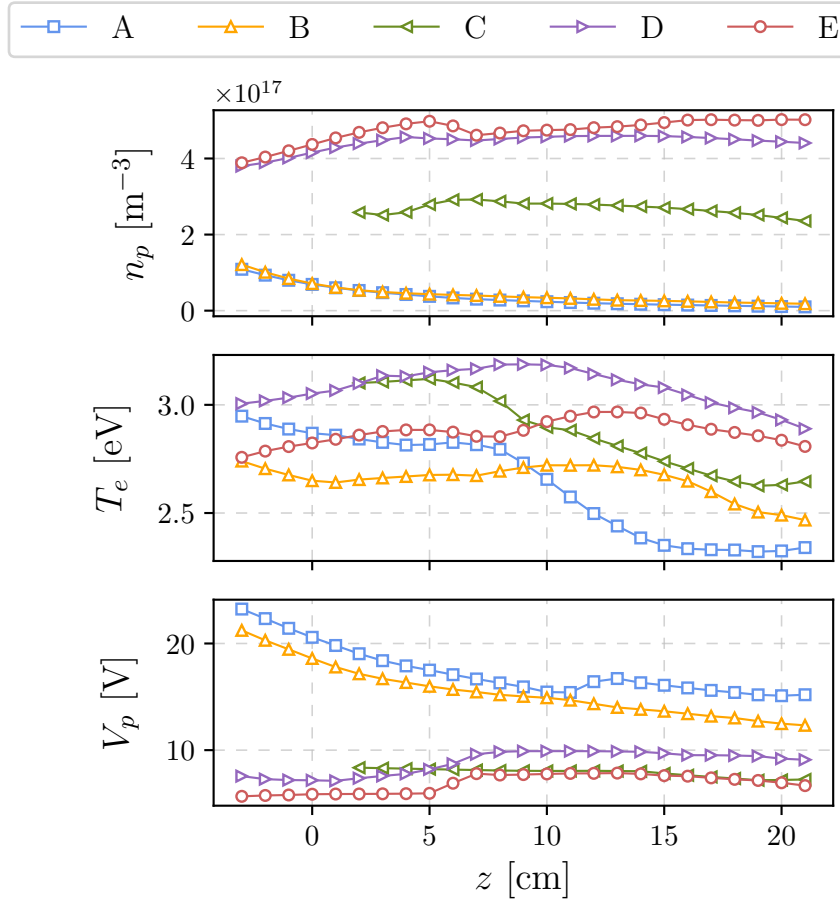
This is the author's peer reviewed, accepted manuscript. However, the online version of record will be different from this version once it has been copyedited and typeset.
PLEASE CITE THIS ARTICLE AS DOI: 10.1063/5.0069983



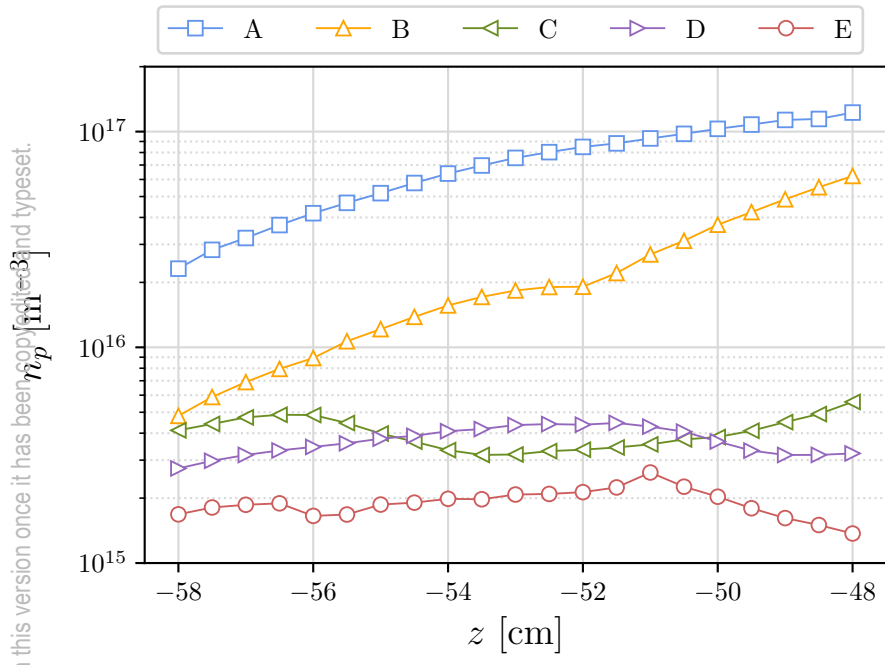
This is the author's peer reviewed, accepted manuscript. However, the online version of record will be different from this version once it has been copyedited and typeset.
PLEASE CITE THIS ARTICLE AS DOI: 10.1063/5.0069983



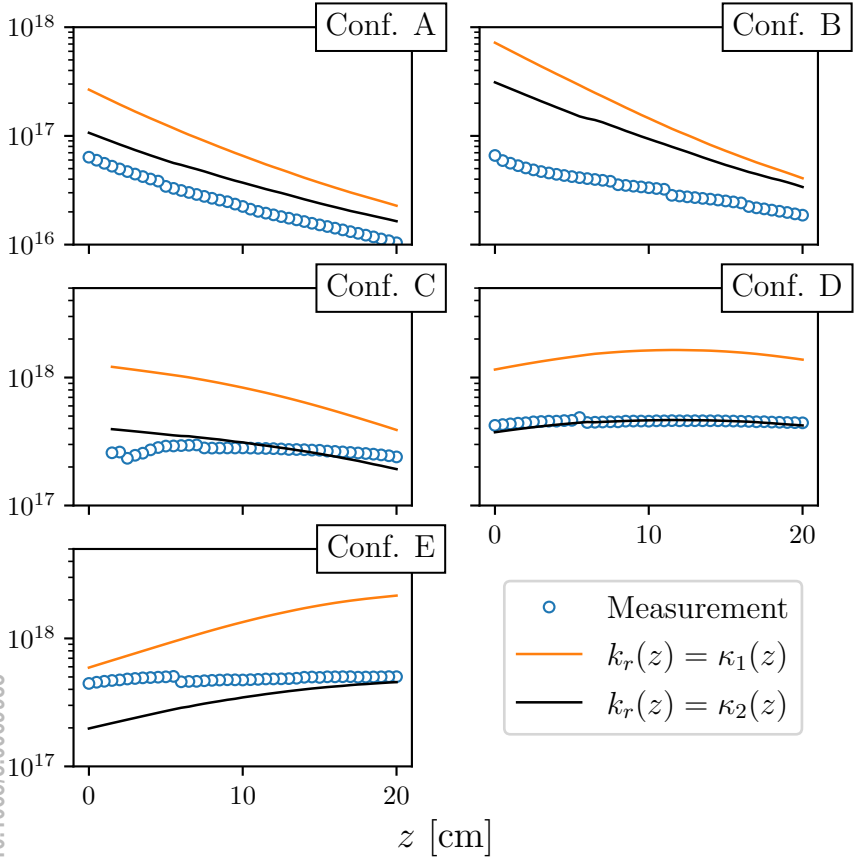
This is the author's peer reviewed, accepted manuscript. However, the online version of record will be different from this version once it has been copyedited and typeset.
PLEASE CITE THIS ARTICLE AS DOI: 10.1063/5.0069983



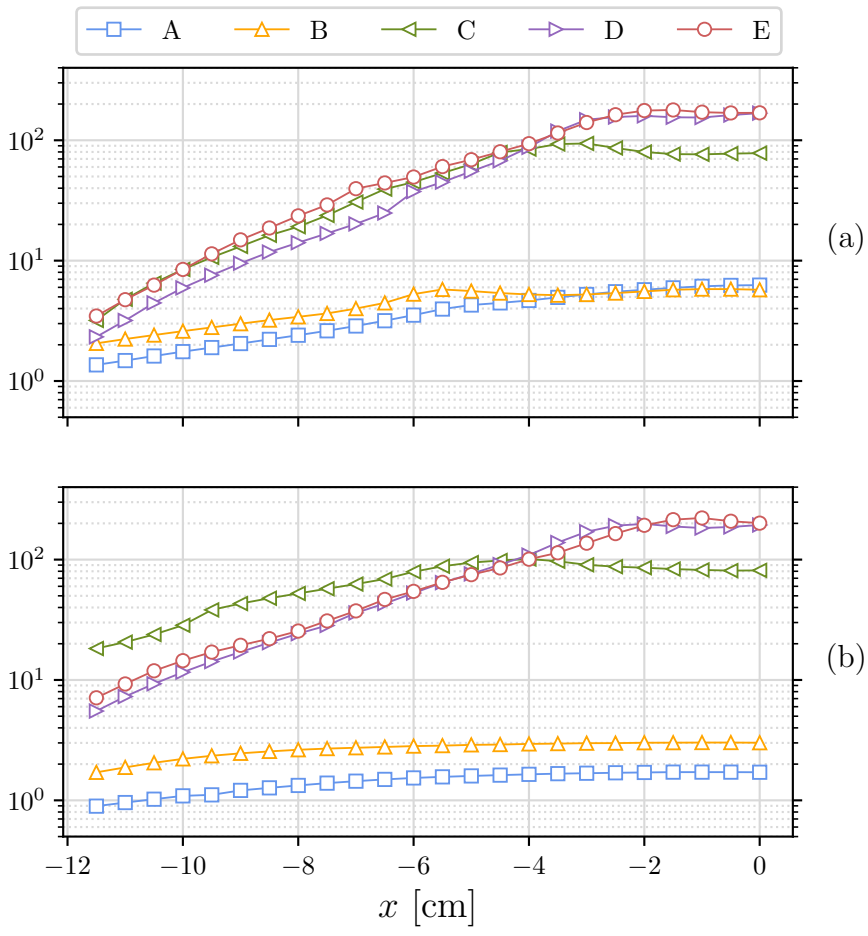
This is the author's peer reviewed, accepted manuscript. However, the online version of record will be different from this version once it has been copyedited and typeset.
PLEASE CITE THIS ARTICLE AS DOI: 10.1063/5.0069983



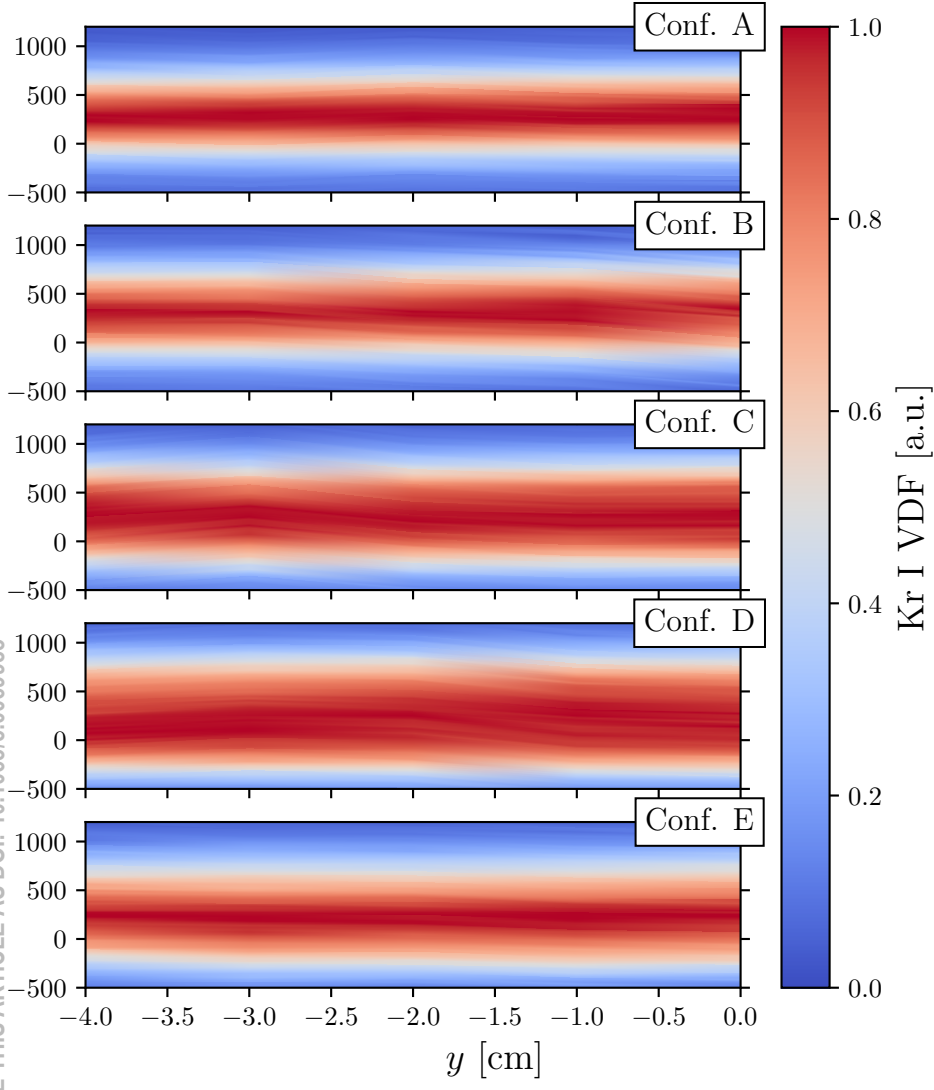
This is the author's peer reviewed, accepted manuscript. However, the online version of record will be different from this version once it has been copyedited and typeset.
PLEASE CITE THIS ARTICLE AS DOI: 10.1063/5.0069983



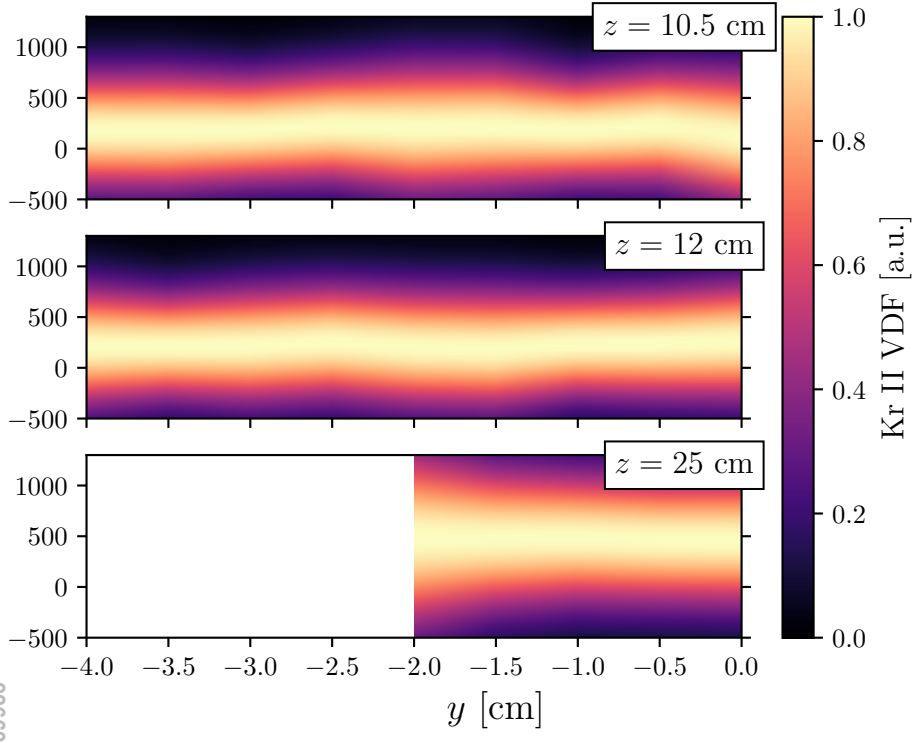
This is the author's peer reviewed, accepted manuscript. However, the online version of record will be different from this version once it has been copyedited and typeset.
PLEASE CITE THIS ARTICLE AS DOI: 10.1063/5.0069983



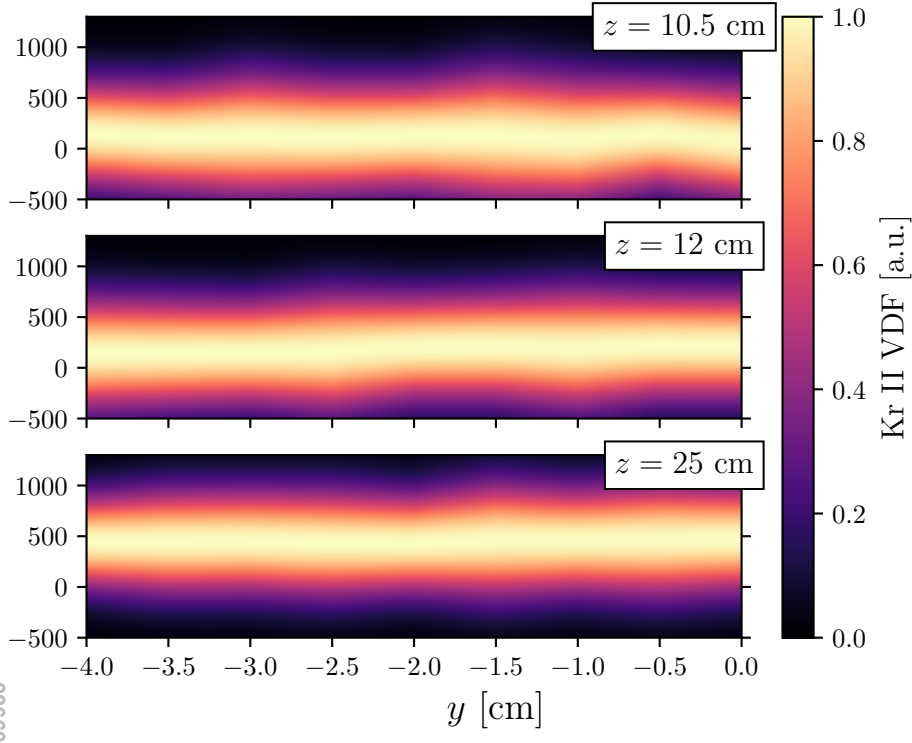
This is the author's peer reviewed, accepted manuscript. However, the online version of record will be different from this version once it has been copyedited and typeset.
PLEASE CITE THIS ARTICLE AS DOI: 10.1063/5.0069983



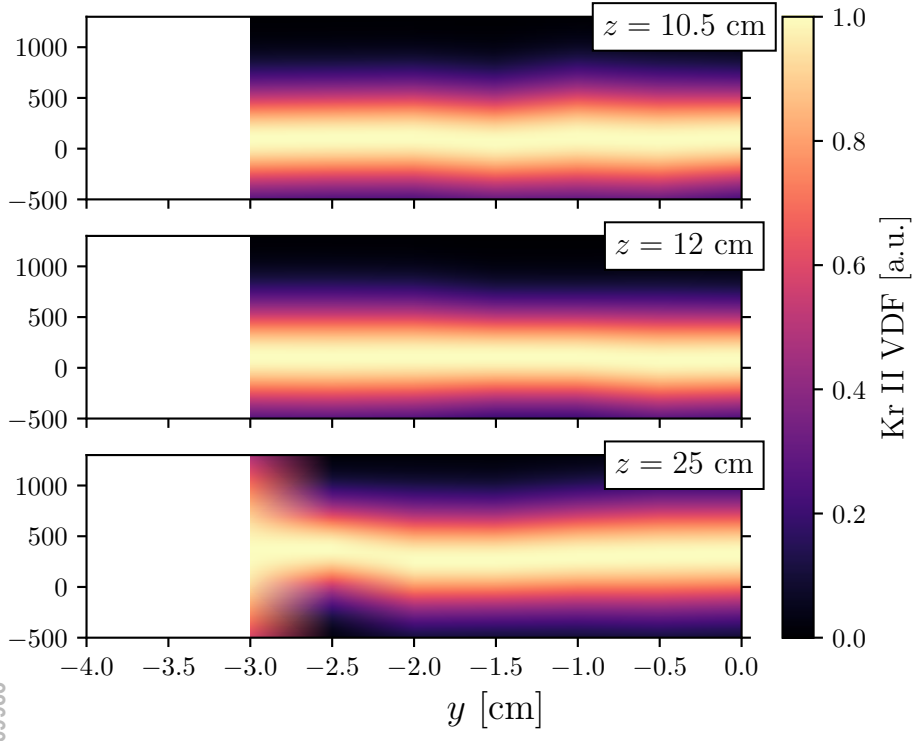
This is the author's peer reviewed, accepted manuscript. However, the online version of record will be different from this version once it has been fully edited and typeset.
PLEASE CITE THIS ARTICLE AS DOI: 10.1063/5.0069983



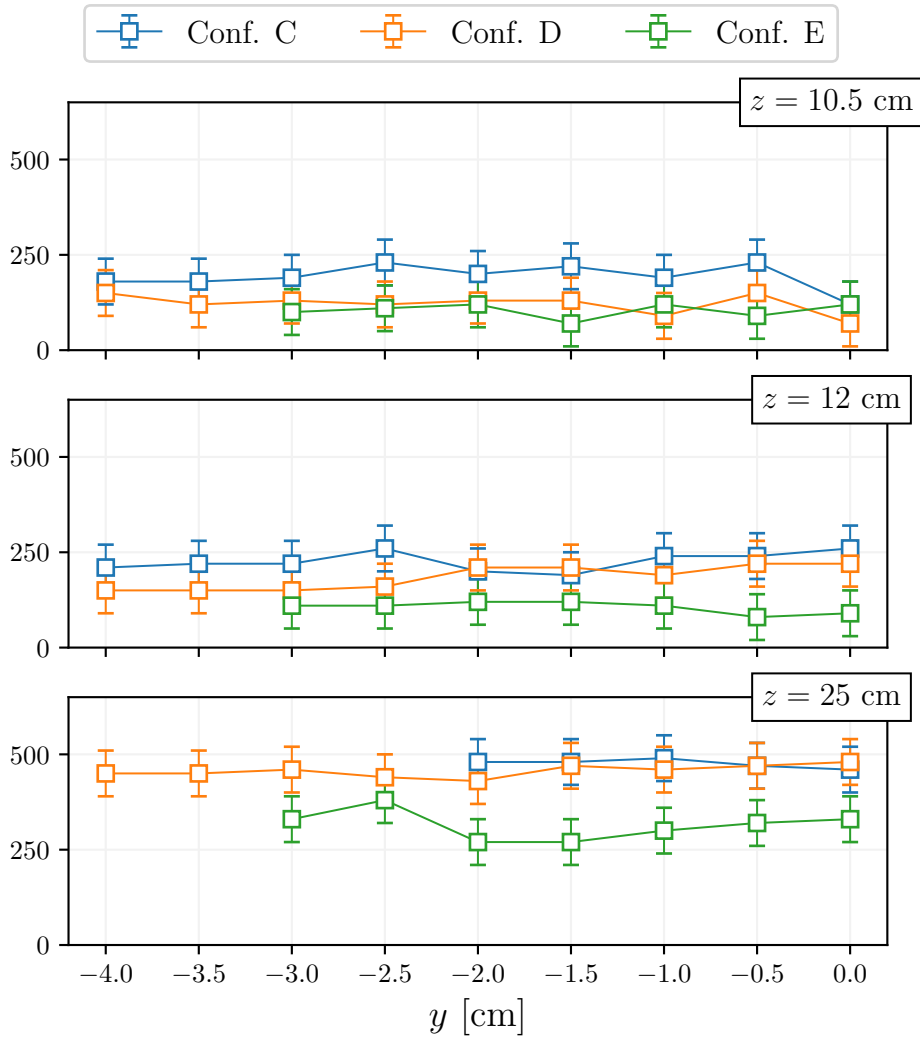
This is the author's peer reviewed, accepted manuscript. However, the online version of record will be different from this version once it has been fully edited and typeset.
PLEASE CITE THIS ARTICLE AS DOI: 10.1063/5.0069983



This is the author's peer reviewed, accepted manuscript. However, the online version of record will be different from this version once it has been fully edited and typeset.
PLEASE CITE THIS ARTICLE AS DOI: 10.1063/5.0069983



This is the author's peer reviewed, accepted manuscript. However, the online version of record will be different from this version because it may have been edited and typeset. PLEASE CITE THIS ARTICLE AS DOI: 10.1063/5.0069983



This is the author's peer reviewed, accepted manuscript. However, the online version of record will be different from this pre-proof. This pre-proof has been copyedited and typeset.
 PLEASE CITE THIS ARTICLE AS DOI: 10.1063/5.0069983

